2008

A Fourier Solution for Electromagnetic Scattering by a Covered Rectangular Cavity

Jessica Moser

A FOURIER SOULUTION FOR ELECTROMAGNETIC SCATTERING BY A COVERED RECTANGULAR CAVITY

A Thesis

Submitted to McAnulty College

and Graduate School of Liberal Arts

Duquesne University

In partial fulfillment of the requirements for

the degree of Masters of Science

By

Jessica L. Moser

July 2008

A FOURIER SOULUTION FOR ELECTROMAGNETIC SCATTERING BY A COVERED RECTANGULAR CAVITY

By

Jessica Moser

Approved July 17, 2008

John Fleming, Ph.D. Assistant Professor of Mathematics (Dissertation Director)	Stacey Levine, Ph.D. Associate Professor of Mathematics (Committee Member)
Mark Mazur, Ph.D. Associate Professor of Mathematics Director of Graduate Study (Committee Member)	Albert C. Labriola , Ph.D. Acting Dean McAnulty College and Graduate School of Liberal Arts

ABSTRACT

A FOURIER SOULUTION FOR ELECTROMAGNETIC SCATTERING BY A COVERED RECTANGULAR CAVITY

By

Jessica L. Moser

July 2008

Thesis Supervised by Dr. John Fleming

This research investigates the plane-wave scattering from a two-dimensional rectangular cavity embedded in an infinite metallic surface that has been covered with a dielectric material. The transverse magnetic and transverse electric polarizations are both considered. The rectangular geometry of the embedded cavity allows for the use of a Fourier based solution. Presented here are modifications to the Fourier solution due to the addition of the material layer above the metallic surface. Applying these modifications allows for a solution to be determined for the electric and magnetic fields at the cavity aperture, where the strength of the return echo is then calculated and displayed in a radar cross section. In addition, an alternate method is introduced to improve upon the speed that it takes to determine a solution, providing a close approximation to the actual results.

ACKNOWLEDGMENT

I would like to first express my deepest gratitude to Dr. John Fleming for all of his assistance, as well as his willingness and patience to educate me with the knowledge to complete this project. The insight and support provided throughout these two years has been invaluable and beyond appreciated.

I am also thankful for the encouragement from my committee members, Dr. Stacey Levine and Dr. Mark Mazur, as well as the faculty members in the Mathematics and Computer Science department at Duquesne University.

Finally, I am extremely grateful for the continous support and encouragement offered by my fiance, Geremie, as well as my family and friends.

Contents

List of Figures

Chapter 1

Introduction

Radar is the technology used to detect and locate various reflecting objects and is well known for its role in the detection of aircrafts, ships and missiles. A radar system emits electromagnetic waves towards a target, and by comparing the strength of the emitted wave to the return echo, displays the results in a radar cross section (RCS). This technology plays a pivotal role in military surveillance and has lead to a major research interest in accurately predicting and controlling these RCS signatures (Skolnik 1990). The RCS of each object is unique, and also dependent on the way in which the wave scatters from its surface, thus it is important to analyze the effect that various surfaces have on the scattering profile. Inconsistencies in a target's surface tend to have significant effects on the RCS signature, and has driven research to focus on the effect of small gaps, cracks and seams on these profiles.

The military utilizes these types of predictions in stealth design, where often the objective is to reduce the total RCS signature by minimizing the scattered energy from the surface of the body. There are also occasions where there is interest in enhancing or altering the expected RCS profile of an object as a defense technique. In either scenario, this can be accomplished by optimizing the design of the aircraft. The body shape and

material coating can alter these signatures, and both factors should be considered when attempting to model accurate predictions.

The prediction of these scattering profiles has also been recognized as a possible nondestructive technique and is currently an important field of study for aircraft maintenance (Blackshire, Buynak, Steffes, and Marshall 2006). Typical maintenance procedures begin with stripping the aircraft surface of its coating in order to perform a visual inspection for signs of fatigue and cracks in the surface. Alternate methods for these inspections have been of interest due to costs associated with the process, and when considering the use of electromagnetic scattering, the ability to account for the material coating in predicting the RCS must be present. Although we have only considered aircraft maintenance, parallel arguments can be made for the maintenance of other large metallic structures, such as bridges and buildings, where cost and time constraints are equally demanding.

There are various influences affecting the outcome of the RCS profile, and all of these possibilities should be considered in developing a model to predict accurately these signatures. Previous literature has determined that even the existence of a small cavity in a metallic surface can have a significant effect on the RCS profile and this paper further explores the effect a material coating over this planar surface has on the RCS profile.

1.1 Statement Of The Problem

A small crack or seam in a metallic surface can be modeled by a rectangular channel in an infinite plane. (See Figure 2.1) This structure is visualized in three dimensions, however the study of similar structures in two dimensions offers computationally efficient approximations. The aim of our research is to investigate the two-dimensional scattering of an incident plane wave off the surface of a metal ground plane that has been completely covered with a dielectric material and contains a rectangular cavity situated at the edge of

a half plane. Since the problem can be decomposed into two dimensions, we are interested in seeking the results when the incident wave is of transverse electric (TE) and transverse magnetic (TM) polarization. Methods to determine the scattering in free space typically involve the use of Green's functions, however, the material layer over the surface and the material inside the cavity adds much complexity to the problem when attempting to find a solution of the wave inside the cavity. An alternate approach is the use of the Fourier transform technique since the plane wave inside the cavity can be written as a sum of exponential functions. In this project, we utilize Fourier transforms to determine a closed form solution of the plane wave inside the cavity space. Then by restricting this solution to the opening of the cavity, the radar cross section of the scattered wave can be determined.

1.2 Related Work

There have been numerous techniques developed to account for the electromagnetic scattering from a cavity-backed aperture in a ground plane, including Fourier transform, finite element, integral equations, cavity mode coupling and impedance boundary conditions. Presented here is the related research and associated techniques that has lead us to the proposed problem.

The Fourier transform technique was utilized by Park and Eom to examine the TE and TM scattering from an empty rectangular cavity embedded in an infinite ground plane (Park, Eom, and Yoshitomi 1992; Park, Eom, and Yoshitomi 1993). This method allowed for a closed form solution to be developed by approximating a series solution for the scattered field. Although this is considered a computationally efficient solution, the methodology is restricted by the shape of the embedded cavity. Since then, various studies have analyzed the effect that filling the rectangular cavity with a dielectric material has on the radar cross section by employing Green's functions, integral equations and impedance boundary conditions (Hoppe and Rahmat-Samii 1995; Barkeshli and Volakis 1989). As these methods tend to be computationally burdensome as the size of the cavity increases,

Morgan approached this problem by implementing a mode coupling method, and solved for a rapid approximation technique by extending the cavity walls using propagating waveguide modes (Morgan 1998). In a similar fashion, this paper presents an equivalent methodology by restricting the coefficients of the Fourier solution to only the diagonal terms to duplicate the fast approximations published by Morgan.

In comparison, the finite element method has the advantage of being able to model arbitrary shaped cavities embedded in a ground plane. Analysis of the TM case of a material filled arbitrarily shaped cavity was analyzed by Wood using a set of scalar integral equations, where Howe's masters thesis expanded this to look at the results of the TE case (Wood 1999; Howe 2001). An alternate solution to this problem was presented by Van and Wood which coupled the finite element method with Fourier transforms, expressing the results of both the TM and TE case (Van and Wood 2003). While these papers provide efficient solutions for an arbitrarily shaped cavity, they are dependent on the ideal situation where the material layer is restricted to the cavity space below the half plane. Wood was able to account for this problem, and extended the research to consider the effect of over filling the cavity space with a dielectric material. This was accomplished by creating an artificial boundary condition on a semi-circle inscribing the overfilled material region, and combining a hybrid finite element method with Fourier transforms to solve for the far field scattering (Wood 2006). This methodology touches upon the possibility of the entire surface being coated with a material layer, however, becomes problematic due to the increasing size of the semi-circle needed to bound the material region.

The work proposed in this paper is an extension of previously published literature, where we are considering an embedded rectangular cavity, in which the entire surface is coated with a dielectric material. Understanding the problem with the restricted cavity shape allows for the boundary conditions to be appropriately defined so that future research can investigate the use of the finite element method to solve for the scattering based on any arbitrary cavity.

1.3 Background

Electromagnetic waves are comprised of electric and magnetic components that oscillate transverse to one another, while also transverse to the direction of propagation. The relationship between these two components is best described mathematically by Maxwell's equations:

$$\nabla \times E = -\frac{\partial(\mu H)}{\partial t} \tag{1.1}$$

$$\nabla \times H = J + \frac{\partial(\varepsilon E)}{\partial t} \tag{1.2}$$

$$\nabla \cdot \varepsilon E = \rho_v \tag{1.3}$$

$$\nabla \cdot \mu H = 0 \tag{1.4}$$

where E and H are the electric and magnetic field, respectively, J is the current density, ε is the permittivity of the medium, μ is the permeability of the medium and ρ_v is the free charge density.

In the problem described, the incident wave is the only source introduced into the problem, as free-space has no current or electric charge by definition, and a dielectric material is a non-conductive substance which also lacks a current and electric charge, thus $J = \rho = 0$. Applying this knowledge while implementing the time harmonic, plane wave form of Maxwell's equation, $e^{\imath wt}$, reduces these equations to:

$$\nabla \times E = -\imath w \mu H \tag{1.5}$$

$$\nabla \times H = \imath w \varepsilon E \tag{1.6}$$

$$\nabla \cdot \varepsilon E = 0 \tag{1.7}$$

$$\nabla \cdot \mu H = 0 \tag{1.8}$$

The wave equation for the electric field can be determined by eliminating the magnetic field from Maxwell's equations. Taking the curl of both side of equation 1.5 results in:

$$\nabla \times \nabla \times E = -\nabla \times iw\mu H$$

Applying the vector identity to the left hand side and substituting in equations 1.6 and 1.7 further reveals that:

$$\begin{aligned} \nabla (\nabla \cdot E) - \nabla^2 (E) &= -\nabla \times iw\mu H \\ \nabla^2 (E) &= -w^2 \mu\varepsilon E \\ \nabla^2 E + k^2 E &= 0 \end{aligned} \tag{1.9}$$

where $k = \sqrt{w^2\mu\varepsilon}$ and represents the wavenumber of the medium. In a similar fashion, the wave equation for the magnetic field can be determined by eliminating the electric field, resulting in:

$$\nabla^2 H + k^2 H = 0 \tag{1.10}$$

In this paper, we are seeking a solution given a two-dimensional model, thus without loss of generality, the entire geometry will be considered invariant in the z direction. The electromagnetic waves can then be described on the xy-plane and are decomposed into two polarizations:

1. If the electric component is perpendicular to the xy-plane, then the magnetic component is parallel to the xy-plane. Together, these two components form the transverse magnetic field.

2. If the electric component is parallel to the xy-plane, then the magnetic component is perpendicular to the xy-plane. Likewise, this situation creates the transverse electric field.

Therefore the two-dimensional scattering of a transverse magnetic incident wave from an object's surface is measured independently of the scattering of a transverse electric incident wave, and the results of each polarization are analyzed independently in chapter eight.

In chapter two, the cavity geometry is explained in detail, along with the boundary conditions affecting the wave at each interface. The results of the magnetic and electric polarizations are analyzed separately in this paper, where the TM case is discussed first in chapters three and four, followed by the TE case in chapters five and six. The two chapters representing each specific polarization is broken down so that the first of the two chapters addresses the simplified problem where there is no material layer above the half plane. The second then addresses the complexity of problem once the material layer is considered in the calculations. Each of these chapters apply the necessary boundary conditions to solve for the coefficients of the Fourier solution, which are then used to solve for the wave at the cavity opening. The radar cross section is then computed in chapter seven based on these results, and the numerical results, which include bistatic and monostatic RCS plots, are provided in chapter eight. Lastly, chapter nine offers the conclusion of this paper with suggested future research.

Chapter 2

Formulation Of the Problem

2.1 Cavity Geometry

Consider a two-dimensional infinite half plane comprised of an idealized metal where no fields can exist within or along its boundaries. Such a material is defined as a perfect electrical conductor (PEC), where any incoming wave is reflected in its entirety at the metal's surface. Let there exist a rectangular cavity of length L and depth d within the half plane, such that the edge of the cavity lies along the edge of the plane. Now consider coating the entire conducting surface, with a thin dielectric material layer. (See Figure 2.1) The half plane above the PEC can then be considered partitioned into two regions. The upper most region, designated as Region I, contains a source-free medium that is time-invariant, homogeneous and linear, with electric permittivity ε_0 and magnetic permeability μ_0. Below is Region II, containing a dielectric material with electric permittivity ε_1 and magnetic permeability μ_1. Additionally, the cavity space below the half plane is defined as Region III, and contains a dielectric material with electric permittivity ε_2 and magnetic permeability μ_2. The thickness of the material layer atop of the ground plane is denoted as a.

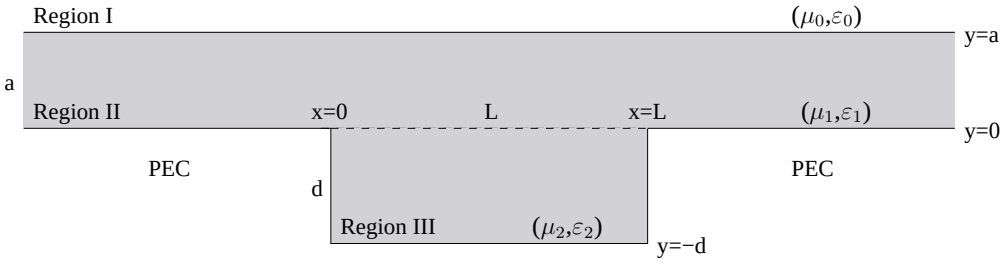

Figure 2.1: Material Covered Plane with Rectangular Cavity

2.2 Boundary Conditions

The scattering of the electromagnetic wave in the far field is a function of the plane wave at the cavity opening, thus the first step in the proposed work is to determine the wave equation at this location. This solution requires careful consideration of the boundary conditions having an affect on the wave. A schematic detailing the incoming, reflected and scattered waves is provided in Figure 2.2. The total electric field of region I, written as E_I, is the summation of all electric fields of the area, where $E_I = E_I^{inc} + E_I^{ref} + E_I^{scat}$. Likewise, the total electric field of region II and III are similarly determined by $E_{II} = E_{II}^{inc} + E_{II}^{ref} + E_{II}^{scat}$ and $E_{III} = E_{III}^{t}$. Similar formulations for the total magnetic fields of each region can be derived.

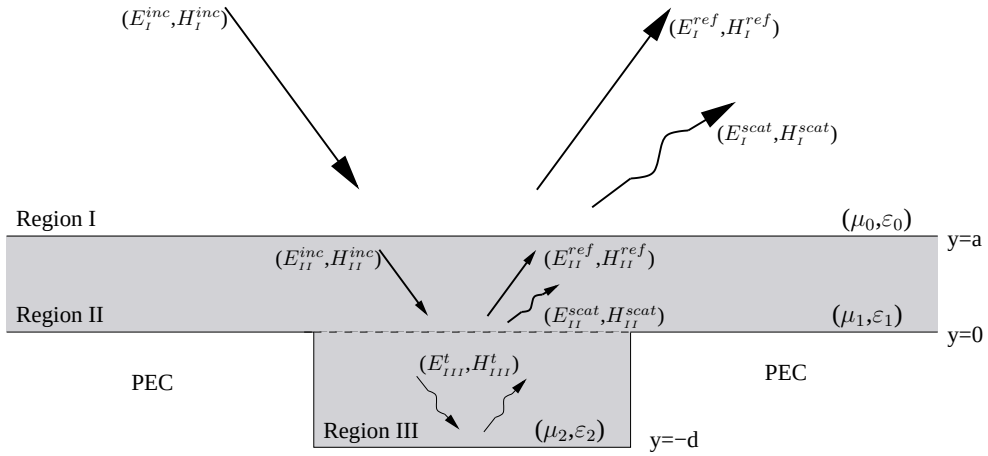

Figure 2.2: Field Representations of the Proposed Geometry

There are imposed boundary conditions at the interface between the two homogeneous regions, where the tangential electric component of a wave is always continuous on crossing a material boundary, and the tangential magnetic component of a wave is continuous across the boundary only if there does not exist a surface current on the boundary. Since we have already established that a surface current does not exist between any of the three regions, the general boundary conditions can be considered:

$$\hat{n} \times (E_I - E_{II}) = 0 \tag{2.1}$$

$$\hat{n} \times (E_{II} - E_{III}) = 0 \tag{2.2}$$

$$\hat{n} \times (H_I - H_{II}) = 0 \tag{2.3}$$

$$\hat{n} \times (H_{II} - H_{III}) = 0 \tag{2.4}$$

where $\hat{n}$ is the normal vector to the surface.

Since the electric fields do not exist within the PEC, the boundary conditions outlined by equations 2.1 and 2.2 reduce to

$$\hat{n} \times E_{II} = 0 \tag{2.5}$$

$$\hat{n} \times E_{III} = 0 \tag{2.6}$$

at the planar surface and inside the cavity walls.

The representation of an electromagnetic wave is dependent on the surrounding constraints and can take on various forms. The geometry in the described problem can be considered a combination of two entities, separated by the half plane. Below the half plane, the electromagnetic wave is bounded by the conducting walls. Above the half plane, the wave is only restricted by the continuity conditions across the material interface. These two representations can be coupled to solve for the Fourier coefficients along the cavity opening and applied to the equation of the wave restricted by the cavity at the opening.

Chapter 3

TM Case - No Material Overlay

Prior to addressing the complexity that a material layer over the entire surface adds to the problem, we will first provide understanding in the simplified case where there exists a filled rectangular cavity at the edge of an infinite PEC, where the region above the half plane is free space. Here we can consider the specifications of region II are equivalent to the specifications of region I. (See Figure 3.1) We will first provide details on how the field equations are determined in each region, then use these wave equations to determine the solution at the cavity opening.

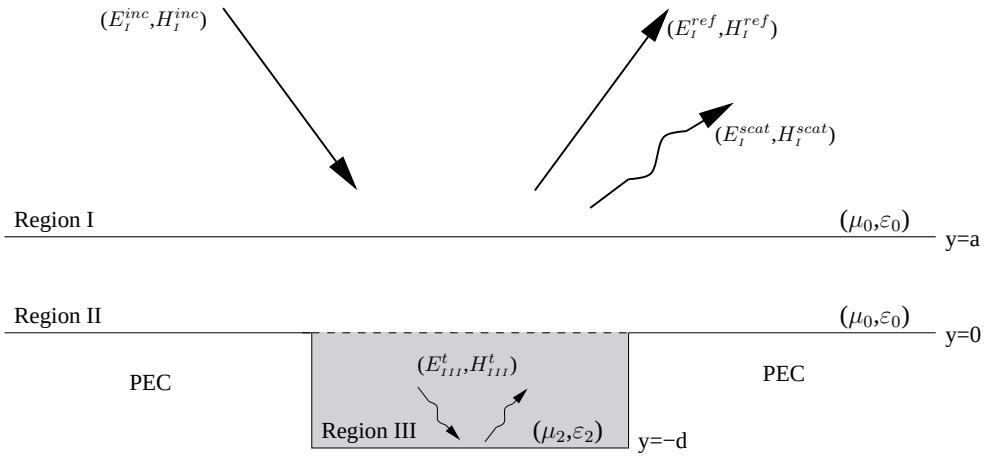

Figure 3.1: Non-Layered Geometry, where material constraints of Region II are equivalent to Region I

3.1 Field Equations

3.1.1 Non-Layered: No Cavity

The effect that an infinite ground plane has on an incoming wave should first be examined prior to considering a surface with an embedded cavity. If no cavity exists below the half plane, the entire incoming wave is reflected at an angle equal to the incoming angle, and only the boundary conditions at the PEC need be considered (Eq. 2.5). Since we are approximating the results in two dimensions where the geometry is z-invariant, the electromagnetic field is then dependent on x and y coordinates of the rectangular Cartesian system. For the readers convenience, the total electric field that is invariant in the z-direction will be denoted as $u(x, y)$ throughout the remainder of this paper, where $u^\imath = \hat{z}E = (0, 0, E_z)$ and $\imath = (0, 1, 2)$ depending on the specified region. The incoming, reflected, scattered and transmitted fields are appropriately denoted as $u^{inc,i}$, $u^{ref,i}$, $u^{scat,i}$ and $u^{t,i}$ respectively. Thus, the general equation for the incoming and reflected wave is:

$$\begin{aligned} u^{inc,0}(x,y) &= e^{\imath k_x^0 x - \imath k_y^0 y} \\ u^{ref,0}(x,y) &= A_{TM}^- e^{\imath k_x^0 x + \imath k_y^0 y} \end{aligned}$$

where A_{TM}^- is a constant term and k_x^0 and k_y^0 represent the direction of propagation and are related to the wavenumber by $(k_x^0)^2 + (k_y^0)^2 = k_0^2$.

The boundary condition specifies that the tangential components of the entire electric field is zero at the surface of the the PEC (where y=0), which allows us to solve for the coefficients in the case of the reflected field:

$$\begin{aligned} u^{inc,0}(x,0) + u^{ref,0}(x,0) &= 0 \\ u^{ref,0}(x,0) &= -u^{inc,0}(x,0) \\ A_{TM}^- e^{\imath k_x^0 x} &= -e^{\imath k_x^0 x} \\ A_{TM}^- &= -1 \end{aligned}$$

Thus, the equation for the incoming and reflected wave for this simplified geometry is:

$$\begin{aligned} u^{inc,0}(x,y) &= e^{\imath k_x^0 x - \imath k_y^0 y} \\ u^{ref,0}(x,y) &= -e^{\imath k_x^0 x + \imath k_y^0 y} \end{aligned}$$

3.1.2 Non-Layered: With Cavity

Now consider the existence of a rectangular cavity situated below the half plane, where the cavity can be either empty or filled with a dielectric material. An incoming electromagnetic field will be transmitted through to the cavity, then scattered back into the far field. Along with the equations representing the incoming and reflected fields determined in section 3.1.1, the equations for transmitted and scattered waves need to be determined.

Since all representations of a wave must satisfy the Helmholtz equation (Eq. 1.9), the method of separation of variables can be implemented to solve for the partial differential equations of the electric field. Using this approach, the electric field is written as a product of two individual functions, where $u(x,y) = \overline{X}(x)\overline{Y}(y)$. Substituting this value in the Helmholtz equation reveals

$$\begin{aligned} \frac{\partial^2 u}{\partial x^2} + \frac{\partial^2 u}{\partial y^2} + k_i^2 u &= 0 \\ \frac{\partial^2 \overline{X}(x)\overline{Y}(y)}{\partial x^2} + \frac{\partial^2 \overline{X}(x)\overline{Y}(y)}{\partial y^2} + k_i^2 \left(\overline{X}(x)\overline{Y}(y)\right) &= 0 \\ \overline{Y}(y)\frac{\partial^2 \overline{X}(x)}{\partial x^2} + \overline{X}(x)\frac{\partial^2 \overline{Y}(y)}{\partial y^2} + k_i^2 \left(\overline{X}(x)\overline{Y}(y)\right) &= 0 \\ \frac{1}{\overline{X}(x)}\frac{\partial^2 \overline{X}(x)}{\partial x^2} + \frac{1}{\overline{Y}(y)}\frac{\partial^2 \overline{Y}(y)}{\partial y^2} + k_i^2 &= 0 \\ \frac{1}{\overline{X}(x)}\frac{\partial^2 \overline{X}(x)}{\partial x^2} &= -\frac{1}{\overline{Y}(y)}\frac{\partial^2 \overline{Y}(y)}{\partial y^2} - k_i^2 \end{aligned}$$

where $k_i = w\sqrt{\varepsilon_i \mu_i}$ and represents wave number within each region and $\imath = (0,1,2)$.

Note that for this statement to be true for all values of x and y, they must be constant functions, which can be represented by $-\lambda$. The boundary conditions of each region can then be enforced to find a solution of the wave within each region.

Solving the general solution for $\overline{\underline{X}}(x)$:

$$\begin{aligned} \frac{1}{\overline{\underline{X}}(x)}\frac{\partial^2\overline{\underline{X}}(x)}{\partial x^2} &= -\lambda \\ \frac{\partial^2\overline{\underline{X}}(x)}{\partial x^2} &= -\lambda\overline{\underline{X}}(x) \end{aligned}$$

Periodic functions solve this type of system where the second derivative returns the negative of the original function. Therefore:

$$\overline{\underline{X}}(x) = C_1 \sin\left(\sqrt{\lambda}x\right) + C_2 \cos\left(\sqrt{\lambda}x\right) \tag{3.1}$$

where C_1 and C_2 are constant terms.

Solving the general solution for $\overline{\underline{Y}}(y)$:

$$\begin{aligned} -\frac{1}{\overline{\underline{Y}}(y)}\frac{\partial^2\overline{\underline{Y}}(y)}{\partial y^2} - k_i^2 &= -\lambda \\ \frac{\partial^2\overline{\underline{Y}}(y)}{\partial y^2} &= (\lambda - k_i^2)\overline{\underline{Y}}(y) \end{aligned}$$

Exponential functions solve this type of system where the second derivative returns some factor of itself. Therefore, the general solution is

$$\overline{\underline{Y}}(y) = C_3 e^{-\sqrt{\lambda - k_i^2}y} + C_4 e^{\sqrt{\lambda - k_i^2}y} \tag{3.2}$$

where C_3 and C_4 are constant terms.

Applying the boundary conditions that are specific to the transmitted and scattered regions allows us to find a solution for each. We will first address the calculations to determine the solution of the transmitted region, then follow with the details of the scattered equation.

Equation of Wave Inside the Cavity, $u^{t,2}(x,y)$:

Previously discussed, the tangential components of an electric field vanish at the surface of the PEC. Thus, the electric component of the periodic function is restricted on the interval $(0, L)$, where $\overline{\underline{X}}(0) = \overline{\underline{X}}(L) = 0$, and can be represented as a superposition of sinusoidal functions. Applying the boundary condition $x = 0$ leads to the conclusion that the constant $C_2 = 0$, reducing equation 3.1 to:

$$\overline{\underline{X}}(x) \;=\; C_1 \sin\left(\sqrt{\lambda}x\right)$$

For the boundary condition to remain true when $x = L$, it must follow that $\sqrt{\lambda}L = n\pi$, thus the equation for the x-component of the transmitted wave is:

$$\overline{\underline{X}}(x) \;=\; C_1 \sin\left(\frac{n\pi}{L}x\right)$$

The solution inside the cavity can then be considered:

$$\begin{aligned} u^{t,2}(x,y) &= \overline{\underline{X}}(x)\overline{\underline{Y}}(y) \\ &= \sum_{n=1}^{\infty} C_n \sin\left(\frac{n\pi}{L}x\right)\left(e^{-\gamma_2 y} + e^{\gamma_2 y}\right) \end{aligned}$$

where $\gamma_2 = \sqrt{\left(\frac{n\pi}{L}\right)^2 - k_2^2}$.

As the electric component also vanishes when $y = -d$, this condition can be applied such that $u^{t,2}(x,-d) = 0$ and reconfiguring the equation in terms of sine and cosine simplifies the representation inside the cavity to:

$$u^{t,2}(x,y) \;=\; \sum_{n=1}^{\infty} A_n^{TM} \sin\left(\frac{n\pi}{L}x\right)\sinh(\gamma_2(y+d)) \tag{3.3}$$

Equation of Scattered Wave of Region I, $u^{scat,0}(x,y)$:

Altering the x-component of the general equation (3.1) in terms of exponentials reveals:

$$\overline{\underline{X}}(x) \quad = \quad C_5 e^{i\sqrt{\lambda}x} + C_6 e^{-i\sqrt{\lambda}x} \tag{3.4}$$

where C_5 and C_6 are constants. The value of λ is restricted such that $\lambda \geq 0$ to assure that the exponential values remain complex. The PEC is considered an infinite plane, so the domain consists of all reals. Since the function is evaluated over all real numbers, we can reduce the equation to eliminate duplicate values as the function is comprised of two components that are inverses of each other. Therefore, we can represent the x-component as:

$$\overline{\underline{X}}(x) \quad = \quad C_7 e^{i\sqrt{\lambda}x}$$

where C_7 is a constant.

Although the scattered wave of region I is not in a bounded region, y is restricted as it gets increasingly large, where $\lim_{y\to\infty} |u^{scat,0}| < \infty$. Under these conditions, for equation 3.2 to result in a zero value, C_4 must be zero, leaving the y-component as:

$$\overline{\underline{Y}}(y) \quad = \quad C_3 e^{-\sqrt{\lambda - k_0^2}y}$$

Combining these two results, the solution of the scattered wave thus far is:

$$\begin{aligned} u^{scat,0}(x,y) &= \overline{\underline{X}}(x)\overline{\underline{Y}}(y) \\ &= C_\lambda e^{\imath\sqrt{\lambda}x} e^{-\sqrt{\lambda - k_0^2}y} d\lambda \end{aligned}$$

Scaling the lambda value such that $\lambda = (2\pi\lambda)^2$ changes the restriction on λ from only positive values to all real values. Thus, instead of the superposition principle applied in the cavity, the solution can be found by integrating over all values of λ.

$$u^{scat,0}(x,y) = \int_{-\infty}^{\infty} D_{TM}(\lambda)\, e^{-\alpha_0 y} e^{2\pi\imath\lambda x} d\lambda \tag{3.5}$$

where $\alpha_0 = \sqrt{(2\pi\lambda)^2 - k_0^2}$.

The general equations for the electric components of the electromagnetic waves within each region are then as follows:

$$u^{inc,0}(x,y) = e^{\imath k_x^0 x - \imath k_y^0 y} \tag{3.6}$$

$$u^{ref,0}(x,y) = -e^{\imath k_x^0 x + \imath k_y^0 y} \tag{3.7}$$

$$u^{scat,0}(x,y) = \int_{-\infty}^{\infty} D_{TM}(\lambda)\, e^{-\alpha_0 y} e^{2\pi\imath\lambda x} d\lambda \tag{3.8}$$

$$u^{t,2}(x,y) = \sum_{n=1}^{\infty} A_n^{TM} \sin\left(\frac{n\pi}{L}x\right) \sinh\left(\gamma_2(y+d)\right) \tag{3.9}$$

3.2 Satisfying the Boundary Conditions

The wave equations of each region have now been determined, and the boundary conditions must be taken into consideration to assure continuity between each of the regions. In this geometry, there exists only one boundary at the cavity aperture between region I and region III when $y = 0$. Since we have eliminated region II by allowing the material constraints to be equivalent to those of region I, the boundary conditions described in section 2.2 reduce to two overall constraints:

$$\hat{n} \times (E_I - E_{III}) = 0 \tag{3.10}$$

$$\hat{n} \times (H_I - H_{III}) = 0 \tag{3.11}$$

Applying the first boundary condition (Eq. 3.10) when $y = 0$ yields a solution for the coefficient $D_{TM}(\lambda)$:

$$
\begin{aligned}
u^0(x,0) &= u^2(x,0) \\
u^{inc,0}(x,0) + u^{ref,0}(x,0) + u^{scat,0}(x,0) &= u^{t,2}(x,0) \\
u^{scat,0}(x,0) &= u^{t,2}(x,0) \qquad \text{applying Eq. 2.5} \\
\int_{-\infty}^{\infty} D_{TM}(\lambda)\, e^{2\pi\imath\lambda x} d\lambda &= \sum_{n=1}^{\infty} A_n^{TM} \sin\left(\frac{n\pi}{L}x\right) \sinh(\gamma_2 d) \\
\mathcal{F}^{-1}\left(D_{TM}(\lambda)\right) &= \sum_{n=1}^{\infty} A_n^{\tilde{TM}} \sin\left(\frac{n\pi}{L}x\right) \\
D_{TM}(\lambda) &= \sum_{n=1}^{\infty} A_n^{\tilde{TM}} \mathcal{F}\left(\sin\left(\frac{n\pi}{L}x\right)\right) \qquad (3.12)
\end{aligned}
$$

where $A_n^{\tilde{TM}} = A_n^{TM} \sinh(\gamma_2 d)$.

The relationship between the electric and magnetic field was previously addressed by Maxwell's equations (Eq. 1.5) . By applying this definition, the general solution for the magnetic field for the TM polarization is determined by:

$$
\begin{aligned}
\nabla \times E &= -\imath w \mu_i H \\
H &= \frac{-1}{\imath w \mu_i} (\nabla \times E) \\
&= \frac{-1}{\imath w \mu_i} (\nabla \times u(x,y)) \\
&= \frac{-1}{\imath w \mu_i} \left(\frac{\partial u}{\partial y}(x,y)\right) \qquad (3.13)
\end{aligned}
$$

Now, applying the boundary condition related to the continuity of the magnetic field specified by equation 3.11 when $y = 0$ reveals:

$$\begin{aligned}
\frac{-1}{\imath w\mu_0}\frac{\partial u^0}{\partial y}(x,0) &= \frac{-1}{\imath w\mu_2}\frac{\partial u^2}{\partial y}(x,0) \\
\mu_2\frac{\partial u^{inc,0}}{\partial y}(x,0)+\mu_2\frac{\partial u^{ref,0}}{\partial y}(x,0)+\mu_2\frac{\partial u^{scat,0}}{\partial y}(x,0) &= \mu_0\frac{\partial u^{t,2}}{\partial y}(x,0) \\
-2\mu_2\imath k_y^0 e^{\imath k_x^0 x}-\mu_2\int_{-\infty}^{\infty} D_{TM}(\lambda)\,\alpha_0 e^{2\pi\imath\lambda x}d\lambda &= \mu_0\sum_{n=1}^{\infty} A_n^{TM}\gamma_2\sin\left(\frac{n\pi}{L}x\right)\cosh(\gamma_2 d) \\
2\mu_2\imath k_y^0 e^{\imath k_x^0 x}+\mu_2\mathcal{F}^{-1}\left(D_{TM}(\lambda)\,\alpha_0\right) &= -\mu_0\sum_{n=1}^{\infty} A_n^{\tilde{TM}}\gamma_2\sin\left(\frac{n\pi}{L}x\right)\coth(\gamma_2 d)
\end{aligned}$$

Since all terms of a Fourier Series are mutually orthogonal, the equation can be reduced to:

$$\begin{aligned}
2\mu_2\imath k_y^0\int_0^L e^{\imath k_x^0 x}\sin\left(\frac{m\pi}{L}x\right)dx+\mu_2\int_0^L \mathcal{F}^{-1}\left(D_{TM}(\lambda)\,\alpha_0\right)\sin\left(\frac{m\pi}{L}x\right)dx \\
= -\mu_0\frac{L}{2}A_m^{\tilde{TM}}\gamma_{2m}\coth(\gamma_{2m}d)
\end{aligned}$$

where $\gamma_{2m}=\sqrt{\left(\frac{m\pi}{L}\right)^2-k_2^2}$ and $A_m^{\tilde{TM}}=A_m^{TM}\sinh(\gamma_{2m}d)$.
Performing a straight integration and utilizing Parseval's Theorem further results in:

$$\begin{aligned}
\mu_2 k_y^0\left(\frac{e^{\imath k_x^0+\imath m\pi}-1}{\frac{\imath m\pi}{L}+\imath k_x^0}-\frac{e^{\imath k_x^0-\imath m\pi}-1}{\frac{\imath m\pi}{L}-\imath k_x^0}\right)+\mu_2\int_{-\infty}^{\infty} D_{TM}(\lambda)\,\alpha_0\overline{\mathcal{F}\left(\sin\left(\frac{m\pi}{L}x\right)\right)}d\lambda \\
= -\mu_0\frac{L}{2}A_m^{\tilde{TM}}\gamma_{2m}\coth(\gamma_{2m}d)
\end{aligned}$$

Lastly, substituting in the known values for $D_{TM}(\lambda)$ determined in equation 3.12 and rearranging the solution yields:

$$\begin{aligned}
\sum_{n=1}^{\infty} A_n^{\tilde{TM}}\int_{-\infty}^{\infty}\alpha_0\mathcal{F}\left(\sin\left(\frac{n\pi}{L}x\right)\right)\overline{\mathcal{F}\left(\sin\left(\frac{m\pi}{L}x\right)\right)}d\lambda+\mu_{r2}\frac{L}{2}A_m^{\tilde{TM}}\gamma_{2m}\coth(\gamma_{2m}d) \\
= k_y^0\left(\frac{e^{\imath k_x^0-\imath m\pi}-1}{\frac{\imath m\pi}{L}-\imath k_x^0}-\frac{e^{\imath k_x^0+\imath m\pi}-1}{\frac{\imath m\pi}{L}+\imath k_x^0}\right)
\end{aligned} \tag{3.14}$$

where μ_{r2} is the relative permeability of region III to that of free-space.

The coefficients of the Fourier solution, $\tilde{A_n^{TM}}$, that satisfy this equation for every field form an infinite system of linear equations. In order to solve for the coefficients computationally, it is required that the series be truncated. We are able to perform this action because it is known that in a Fourier-based solution, as the number of unknowns used in the system of linear equation increases, the truncated series will converge (Fleming 2008). The resulting effect is an $n \times n$ matrix representing the data values on the left hand side of equation 3.14, and an $n \times 1$ matrix representing the data values on the right hand side, which allows us to solve for the Fourier coefficients. As the number of unknowns used to find the solution increases, the computational time increases by a factor of n^2. Although we have implemented this methodology in our work, we have also investigated increasing the speed of the computation time by reducing the matrix defined for the left hand side to a strict diagonal matrix. This yields a rapid approximation technique, which provides results similar to those published by Morgan (Morgan 1998).

Chapter 4

TM Case - Layered

In this chapter, the geometry in chapter three is extended to include a material layer above the half plane. (See Figure 4.1) Here we will analyze how the introduction of the this layer affects the field equations, and using this information, solve for the Fourier coefficients along the cavity aperture. Again, a solution for the incoming and reflected waves is determined in section 4.1.1 by analyzing the behavior when the geometry lacks a cavity below the surface. Once these field equations have been established, section 4.1.2 analyzes the changes caused by the cavity's existence. Then in section 4.2, the boundary conditions are enforced in order to find a solution for the Fourier coefficients.

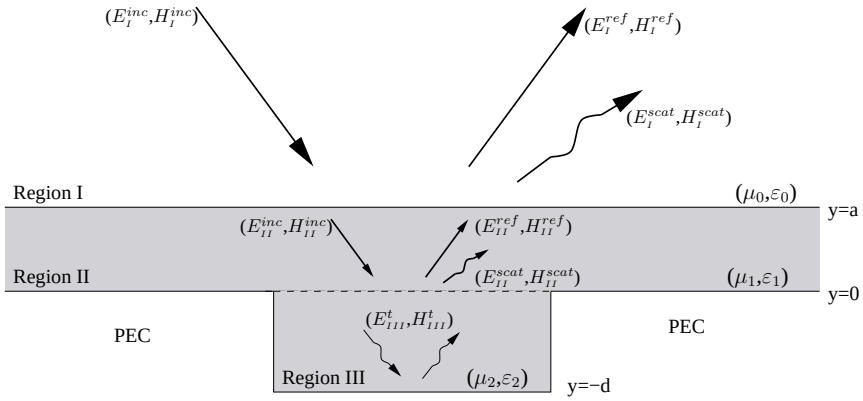

Figure 4.1: Layered Geometry

4.1 Field Equations

4.1.1 Layered: No Cavity

Although there is no cavity below the half plane, the equations governing the incoming and reflected waves increase in complexity because of the extra layer. The change in material that the wave encounters has an affect on the speed and angle of refraction, which is dependent on the permittivity and permeability of the medium. This change is accounted for in the coefficients of the field equations in each region, where the incoming and reflected wave of region I is again modeled as

$$\begin{aligned} u^{inc,0}(x,y) &= e^{\imath k_x^0 x - \imath k_y^0 y} \\ u^{ref,0}(x,y) &= A_{TM}^- e^{\imath k_x^0 x + \imath k_y^0 y} \end{aligned}$$

Due to the slight change in the wave in region II, the equation of the incident and reflected wave is modified by a constant factor, which we represent by B_{TM}^+ and B_{TM}^-,

$$\begin{aligned} u^{inc,1}(x,y) &= B_{TM}^+ e^{\imath k_x^1 x - \imath k_y^1 y} \\ u^{ref,1}(x,y) &= B_{TM}^- e^{\imath k_x^1 x + \imath k_y^1 y} \end{aligned}$$

where k_x^1 and k_y^1 are related to the wavenumber of region II by $(k_x^1)^2 + (k_y^1)^2 = k_1^2$.

The boundary condition related to the PEC still applies, such that the tangential components of the total electric field in region II are zero. Enforcing this boundary condition allows us to eliminate one of the unknown coefficients.

$$\begin{aligned} u^1(x,0) &= 0 \qquad (4.1) \\ u^{inc,1}(x,0) + u^{ref,1}(x,0) &= 0 \\ B_{TM}^+ e^{\imath k_x^1 x} &= -B_{TM}^- e^{\imath k_x^1 x} \\ B_{TM}^+ &= -B_{TM}^- \end{aligned}$$

In order to solve for the remaining unknown constants representing the change in behavior of the incoming and reflected plane waves, the boundary condition of the material interface at $y = a$ must be enforced. Applying the condition related to the electric field specified by equation 2.1 yields:

$$\begin{aligned} u^0(x,a) &= u^1(x,a) \\ u^{inc,0}(x,a) + u^{ref,0}(x,a) &= u^{inc,1}(x,a) + u^{ref,1}(x,a) \\ e^{\imath k_x^0 x - \imath k_y^0 a} + A_{TM}^- e^{\imath k_x^0 x + \imath k_y^0 a} &= B_{TM}^+ \left(e^{\imath k_x^1 x - \imath k_y^1 a} - e^{\imath k_x^1 x + \imath k_y^1 a} \right) \end{aligned} \tag{4.2}$$

The magnetic field can again be computed by applying equation 3.13, and by enforcing the related boundary condition as specified by equation 2.2, reveals:

$$\begin{aligned} \frac{-1}{\imath w \mu_0} \frac{\partial u^0}{\partial y}(x,a) &= \frac{-1}{\imath w \mu_1} \frac{\partial u^1}{\partial y}(x,a) \\ \mu_1 \frac{\partial u^{inc,0}}{\partial y}(x,a) + \mu_1 \frac{\partial u^{ref,0}}{\partial y}(x,a) &= \mu_0 \frac{\partial u^{inc,1}}{\partial y}(x,a) + \mu_0 \frac{\partial u^{ref,1}}{\partial y}(x,a) \\ -\imath k_y^0 \mu_1 e^{\imath k_x^0 x - \imath k_y^0 a} + \imath k_y^0 \mu_1 A_{TM}^- e^{\imath k_x^0 x + \imath k_y^0 a} &= -\imath k_y^1 \mu_0 B_{TM}^+ \left(e^{\imath k_x^1 x - \imath k_y^1 a} + e^{\imath k_x^1 x + \imath k_y^1 a} \right) \end{aligned} \tag{4.3}$$

These results provide us a system of equations in two unknowns that can be solved for, where

$$A_{TM}^- = \frac{e^{-2\imath k_y^0 a} \left(k_y^0 \mu_{r1} \left(e^{-\imath k_y^1 a} - e^{\imath k_y^1 a} \right) - k_y^1 \left(e^{-\imath k_y^1 a} + e^{\imath k_y^1 a} \right) \right)}{k_y^1 \left(e^{-\imath k_y^1 a} + e^{\imath k_y^1 a} \right) + k_y^0 \mu_{r1} \left(e^{-\imath k_y^1 a} - e^{\imath k_y^1 a} \right)} \tag{4.4}$$

$$B_{TM}^+ = \frac{2 k_y^0 \mu_{r1} e^{-\imath k_y^0 a}}{k_y^1 \left(e^{-\imath k_y^1 a} + e^{\imath k_y^1 a} \right) + k_y^0 \mu_{r1} \left(e^{-\imath k_y^1 a} - e^{\imath k_y^1 a} \right)} \tag{4.5}$$

and μ_{r1} is the relative permeability of region II to that of free space.

4.1.2 Layered: With Cavity

We now consider the problem of the TM case of an incident plane wave impinging on a rectangular cavity embedded in an infinite ground plane that has been entirely coated with a dielectric material. (See Figure 2.2) The field equations representing the incident and reflective waves of regions I and II were outlined in section 4.1.1, however the existence

of the buried cavity also results in the need to calculate the equation of the transmitted wave of region III and the equations for scattered waves of regions I and II.

Similar to the non-layered cavity problem presented in section 3.1.2, the scattering equation of Region I is:

$$u^{scat,0}(x,y) \;=\; \int_{-\infty}^{\infty} D_{TM}\left(\lambda\right) e^{-\alpha_0 y} e^{2\pi\imath\lambda x} d\lambda$$

Since region II is bounded both above and below, the scattering in both the positive and negative directions must be accounted for, and is represented by:

$$u^{scat,1}(x,y) \;=\; \int_{-\infty}^{\infty} \left(G_{TM}\left(\lambda\right) e^{-\alpha_1 y} + H_{TM}\left(\lambda\right) e^{\alpha_1 y}\right) e^{2\pi\imath\lambda x} d\lambda$$

where $\alpha_1 = \sqrt{\left(2\pi\lambda\right)^2 - k_1^2}$

Lastly, applying the logic presented in section 3.1.2 to calculate the transmitted field inside the cavity reveals the same equation, where:

$$u^{t,2}(x,y) \;=\; \sum_{n=1}^{\infty} A_n^{TM} \sin\left(\frac{n\pi}{L}x\right) \sinh\left(\gamma_2(y+d)\right)$$

Thus the general equations for the electric component of the field satisfying the boundary constraint for each region are:

$$u^{inc,0}(x,y) = e^{\imath k_x^0 x - \imath k_y^0 y} \tag{4.6}$$

$$u^{ref,0}(x,y) = A_{TM}^{-} e^{\imath k_x^0 x + \imath k_y^0 y} \tag{4.7}$$

$$u^{scat,0}(x,y) = \int_{-\infty}^{\infty} D_{TM}(\lambda)\, e^{-\alpha_0 y} e^{2\pi\imath\lambda x} d\lambda \tag{4.8}$$

$$u^{inc,1}(x,y) = B_{TM}^{+} e^{\imath k_x^1 x - \imath k_y^1 y} \tag{4.9}$$

$$u^{ref,1}(x,y) = B_{TM}^{-} e^{\imath k_x^1 x + \imath k_y^1 y} = -B_{TM}^{+} e^{\imath k_x^1 x + \imath k_y^1 y} \tag{4.10}$$

$$u^{scat,1}(x,y) = \int_{-\infty}^{\infty} \left(G_{TM}(\lambda)\, e^{-\alpha_1 y} + H_{TM}(\lambda)\, e^{\alpha_1 y} \right) e^{2\pi\imath\lambda x} d\lambda \tag{4.11}$$

$$u^{t,2}(x,y) = \sum_{n=1}^{\infty} A_n^{TM} \sin\left(\frac{n\pi}{L}x\right) \sinh\left(\gamma_2(y+d)\right) \tag{4.12}$$

4.2 Satisfying the Boundary Conditions

To assure that the wave is continuous at each interface, the multiple boundary conditions described in section 2.2 must be upheld. The following section first addresses the boundary constraints between region I and region II prior to offering additional details for the constraints at the cavity aperture.

4.2.1 Boundary $y = a$

Since the electric and magnetic field are continuous across the material interface, the boundary conditions stated in equations 2.2 and 2.4 must be considered. By first applying

the constraint related to the electric field, we are able to determine a solution for the coefficient $D_{TM}(\lambda)$:

$$\begin{aligned}
u^0(x,a) &= u^1(x,a) \\
u^{inc,0}(x,a)+u^{ref,0}(x,a)+u^{scat,0}(x,a) &= u^{inc,1}(x,a)+u^{ref,1}(x,a)+u^{scat,0}(x,a) \\
u^{scat,0}(x,a) &= u^{scat,1}(x,a) \qquad \text{applying Eq. 4.2} \\
\int_{-\infty}^{\infty} D_{TM}(\lambda)\, e^{-\alpha_0 a} e^{2\pi\lambda x} d\lambda &= \int_{-\infty}^{\infty} \left(G_{TM}(\lambda)\, e^{-\alpha_1 a} + H_{TM}(\lambda)\, e^{\alpha_1 a}\right) e^{2\pi\imath\lambda x} d\lambda \\
\mathcal{F}^{-1}\left(D_{TM}(\lambda)\, e^{-\alpha_0 a}\right) &= \mathcal{F}^{-1}\left(G_{TM}(\lambda)\, e^{-\alpha_1 a} + H_{TM}(\lambda)\, e^{\alpha_1 a}\right) \\
D_{TM}(\lambda)\, e^{-\alpha_0 a} &= G_{TM}(\lambda)\, e^{-\alpha_1 a} + H_{TM}(\lambda)\, e^{\alpha_1 a} \qquad (4.13)
\end{aligned}$$

Next, applying the boundary constraints controlling for the continuity of the magnetic field by Eq. 2.4 at $y = a$ also yields a solution for the coefficient $D_{TM}(\lambda)$.

$$\begin{aligned}
\frac{-1}{\imath w\mu_0}\frac{\partial u^0}{\partial y}(x,a) &= \frac{-1}{\imath w\mu_1}\frac{\partial u^1}{\partial y}(x,a) \\
\mu_1\frac{\partial u^{inc,0}}{\partial y}(x,a) + \mu_1\frac{\partial u^{ref,0}}{\partial y}(x,a) + \mu_1\frac{\partial u^{scat,0}}{\partial y}(x,a) & \\
&= \mu_0\frac{\partial u^{inc,1}}{\partial y}(x,a) + \mu_0\frac{\partial u^{ref,1}}{\partial y}(x,a) + \mu_0\frac{\partial u^{scat,1}}{\partial y}(x,a) \\
\mu_1\frac{\partial u^{scat,0}}{\partial y}(x,a) &= \mu_0\frac{\partial u^{scat,1}}{\partial y}(x,a) \qquad \text{applying Eq. 4.3} \\
-\mu_1\int_{-\infty}^{\infty} D_{TM}(\lambda)\,\alpha_0 e^{-\alpha_0 a} e^{2\pi\imath\lambda x} d\lambda &= \mu_0\int_{-\infty}^{\infty}\alpha_1\left(H_{TM}(\lambda)\, e^{\alpha_1 a} - G_{TM}(\lambda)\, e^{-\alpha_1 a}\right) e^{2\pi\imath\lambda x} d\lambda \\
-\mu_1\mathcal{F}^{-1}\left(\alpha_0 D_{TM}(\lambda)\, e^{-\alpha_0 a}\right) &= \mu_0\mathcal{F}^{-1}\left(\alpha_1\left(H_{TM}(\lambda)\, e^{\alpha_1 a} - G_{TM}(\lambda)\, e^{-\alpha_1 a}\right)\right) \\
-\mu_1\alpha_0 D_{TM}(\lambda)\, e^{-\alpha_0 a} &= \mu_0\alpha_1 H_{TM}(\lambda)\, e^{\alpha_1 a} - \mu_0\alpha_1 G_{TM}(\lambda)\, e^{-\alpha_1 a} \qquad (4.14)
\end{aligned}$$

The results from the boundary condition at $y = a$ then provide a system of equations that can be used to solve for $G_{TM}(\lambda)$ and $H_{TM}(\lambda)$.

$$\begin{aligned}
G_{TM}(\lambda) &= D_{TM}(\lambda)\, e^{-\alpha_0 a}\left(\frac{e^{\alpha_1 a}\left(\mu_0\alpha_1 + \mu_1\alpha_0\right)}{2\mu_0\alpha_1}\right) \qquad (4.15) \\
H_{TM}(\lambda) &= D_{TM}(\lambda)\, e^{-\alpha_0 a}\left(\frac{e^{-\alpha_1 a}\left(\mu_0\alpha_1 - \mu_1\alpha_0\right)}{2\mu_0\alpha_1}\right) \qquad (4.16)
\end{aligned}$$

4.2.2 Boundary $y = 0$

The boundary conditions related to the material interface occurring at the cavity aperture, described by equations 2.1 and 2.3, are now applied to assure continuity across the opening. Again, the behavior of the electric component described by equation 2.1 is analyzed first:

$$\begin{aligned}
u^1(x,0) &= u^2(x,0) \\
u^{inc,1}(x,0) + u^{ref,1}(x,0) + u^{scat,1}(x,0) &= u^{t,2}(x,0) \\
u^{scat,1}(x,0) &= u^{t,2}(x,0) \qquad \text{applying Eq. 2.5} \\
\int_{-\infty}^{\infty} \left(G_{TM}(\lambda) + H_{TM}(\lambda)\right) e^{2\pi\imath\lambda x} d\lambda &= \sum_{n=1}^{\infty} A_n^{TM} \sin\left(\frac{n\pi}{L}x\right) \sinh\left(\gamma_2 d\right) \\
\mathcal{F}^{-1}\left(G_{TM}(\lambda) + H_{TM}(\lambda)\right) &= \sum_{n=1}^{\infty} \tilde{A_n^{TM}} \sin\left(\frac{n\pi}{L}x\right) \\
G_{TM}(\lambda) + H_{TM}(\lambda) &= \sum_{n=1}^{\infty} \tilde{A_n^{TM}} \mathcal{F}\left(\sin\left(\frac{n\pi}{L}x\right)\right) \qquad (4.17)
\end{aligned}$$

The values determined for $G_{TM}(\lambda)$ and $H_{TM}(\lambda)$, as shown in equation 4.15 and 4.16 can be substituted in, further reducing the equation to:

$$D_{TM}(\lambda)\, e^{-\alpha_0 a} \left(\frac{e^{-\alpha_1 a}\left(\mu_0\alpha_1 - \mu_1\alpha_0\right) + e^{\alpha_1 a}\left(\mu_0\alpha_1 + \mu_1\alpha_0\right)}{2\mu_0\alpha_1}\right) = \sum_{n=1}^{\infty} \tilde{A_n^{TM}} \mathcal{F}\left(\sin\left(\frac{n\pi}{L}x\right)\right)$$

and solving for $D_{TM}(\lambda)$ yields:

$$D_{TM}(\lambda)\, e^{-\alpha_0 a} = \frac{2\mu_0\alpha_1 \sum_{n=1}^{\infty} \tilde{A_n^{TM}} \mathcal{F}\left(\sin\left(\frac{n\pi}{L}x\right)\right)}{\mathcal{Q}_{\mathcal{A}}^{\mathcal{TM}}} \qquad (4.18)$$

where

$$\mathcal{Q}_{\mathcal{A}}^{\mathcal{TM}} = e^{-\alpha_1 a}\left(\mu_0\alpha_1 - \mu_1\alpha_0\right) + e^{\alpha_1 a}\left(\mu_0\alpha_1 + \mu_1\alpha_0\right)$$

Next, the boundary constraints controlling for the continuity of the magnetic field across the cavity opening at $y = 0$, determined by Eq 2.3, are analyzed:

$$\begin{aligned}
\frac{-1}{\imath w\mu_1}\frac{\partial u^1}{\partial y}(x,0) &= \frac{-1}{\imath w\mu_2}\frac{\partial u^2}{\partial y}(x,0) \\
\mu_2\frac{\partial u^{inc,1}}{\partial y}(x,0) + \mu_2\frac{\partial u^{ref,1}}{\partial y}(x,0) + \mu_2\frac{\partial u^{scat,1}}{\partial y}(x,0) &= \mu_1\frac{\partial u^{t,2}}{\partial y}(x,0) \\
-2\imath k_y^1\mu_2 B_{TM}^+ e^{\imath k_x^1 x} + \mu_2\int_{-\infty}^{\infty}\alpha_1\left(H_{TM}(\lambda) - G_{TM}(\lambda)\right)e^{2\pi\imath\lambda x}d\lambda & \\
= \mu_1\sum_{n=1}^{\infty}A_n^{TM}\gamma_2\sin\left(\frac{n\pi}{L}x\right)\cosh(\gamma_2 d) & \\
-2\imath k_y^1\mu_2 B_{TM}^+ e^{\imath k_x^1 x} + \mu_2\mathcal{F}^{-1}\left(\alpha_1\big(H_{TM}(\lambda) - G_{TM}(\lambda)\big)\right) & \\
= \mu_1\sum_{n=1}^{\infty}A_n^{\tilde{TM}}\gamma_2\sin\left(\frac{n\pi}{L}x\right)\coth(\gamma_2 d) &
\end{aligned}$$

Again, the values determined in equations 4.15 and 4.16 for $G_{TM}(\lambda)$ and $H_{TM}(\lambda)$ can be substituted into the equation, resulting in:

$$\begin{aligned}
-2\imath k_y^1\mu_2 B_{TM}^+ e^{\imath k_x^1 x} + \mu_2\mathcal{F}^{-1}\left(\alpha_1\left(D_{TM}(\lambda)\,e^{-\alpha_0 a}\frac{\mathcal{Q}_{\mathcal{B}}^{\mathcal{TM}}}{2\mu_0\alpha_1}\right)\right) & \\
= \mu_1\sum_{n=1}^{\infty}A_n^{\tilde{TM}}\gamma_2\sin\left(\frac{n\pi}{L}x\right)\coth(\gamma_2 d) &
\end{aligned}$$

where

$$\mathcal{Q}_{\mathcal{B}}^{\mathcal{TM}} = e^{-\alpha_1 a}(\mu_0\alpha_1 - \mu_1\alpha_0) - e^{\alpha_1 a}(\mu_0\alpha_1 + \mu_1\alpha_0)$$

Since the terms of the Fourier series are all mutually orthogonal, this equation can be reduced to:

$$\begin{aligned}
-2\imath k_y^1\mu_2 B_{TM}^+\int_0^L e^{\imath k_x^1 x}\sin\left(\frac{m\pi}{L}x\right)dx & \\
+\mu_2\int_0^L\mathcal{F}^{-1}\left(D_{TM}(\lambda)\,e^{-\alpha_0 a}\frac{\mathcal{Q}_{\mathcal{B}}^{\mathcal{TM}}}{2\mu_0}\right)\sin\left(\frac{m\pi}{L}x\right)dx & \\
= \mu_1\frac{L}{2}A_m^{\tilde{TM}}\gamma_{2m}\coth(\gamma_{2m}d) &
\end{aligned}$$

Then by performing a straight integration and utilizing Parseval's Theorem, our results show:

$$-k_y^1\mu_2 B_{TM}^+\left(\frac{e^{\imath k_x^1+\imath m\pi}-1}{\imath k_x^1+\frac{\imath m\pi}{L}}+\frac{1-e^{\imath k_x^1-\imath m\pi}}{\imath k_x^1-\frac{\imath m\pi}{L}}\right)$$
$$+\mu_2\int_{-\infty}^{\infty}\left(D_{TM}\left(\lambda\right)e^{-\alpha_0 a}\frac{\mathcal{Q}_{\mathcal{B}}^{\mathcal{TM}}}{2\mu_0}\right)\overline{\mathcal{F}\left(\sin\left(\frac{m\pi}{L}x\right)\right)}d\lambda$$
$$=\mu_1\frac{L}{2}A_m^{\tilde{TM}}\gamma_{2m}\coth\left(\gamma_{2m}d\right)$$

Lastly, the values for $D_{TM}\left(\lambda\right)$ calculated in equation 4.18 can be substituted in, and rearranging the equation results in:

$$\sum_{n=1}^{\infty}A_n^{\tilde{TM}}\int_{-\infty}^{\infty}\alpha_1\frac{\mathcal{Q}_{\mathcal{B}}^{\mathcal{TM}}}{\mathcal{Q}_{\mathcal{A}}^{\mathcal{TM}}}\mathcal{F}\left(\sin\left(\frac{n\pi}{L}x\right)\right)\overline{\mathcal{F}\left(\sin\left(\frac{m\pi}{L}x\right)\right)}d\lambda-\frac{\mu_1}{\mu_2}\frac{L}{2}A_m^{\tilde{TM}}\gamma_{2m}\coth\left(\gamma_{2m}d\right)$$
$$=k_y^1 B_{TM}^+\left(\frac{e^{\imath k_x^1+\imath m\pi}-1}{\imath k_x^1+\frac{\imath m\pi}{L}}+\frac{1-e^{\imath k_x^1-\imath m\pi}}{\imath k_x^1-\frac{\imath m\pi}{L}}\right) \tag{4.19}$$

The Fourier coefficients, $A_n^{\tilde{TM}}$, form a system of equations that are solved for computationally by truncating the infinite sum to an arbitrarily large number. These solutions are then applied to solve for the equation at the cavity aperture.

Chapter 5

TE Case - No Material Overlay

In this chapter, the TE polarization is considered. Similar to chapter three, this section provides results for an incoming plane wave impinging on an embedded rectangular cavity that lies within an infinite ground plane, prior to addressing the complexity such a layer would add in computing the far field scattering in chapter 6. The material constraints of region II can be considered equivalent to the constraints of region I for all calculations in this chapter. Again, the incoming and reflected wave equations are first determined from the geometry lacking a cavity, then this is expanded to show the effect of a cavity embedded in the half plane. (See Figure 3.1)

5.1 Field Equations

5.1.1 Non-Layered: No Cavity

In the TE case, the magnetic field is parallel to the direction of propagation and total magnetic field is denoted as H_z. Similar to the TM case, the notation for the entire magnetic field will be simplified for the readers convenience, such that $v^i(x,y) = \hat{z}H$, where $v^i = v^{inc,i} + v^{ref,i} + v^{scat,i}$ when $i = 0, 1$ or $v^i = v^{t,i}$ when $i = 2$. The total

magnetic field can then be written in terms of x and y, such that the general solution of the magnetic component for the incoming and reflected waves is:

$$\begin{aligned} v^{inc,0}(x,y) &= e^{\imath k_x^0 x - \imath k_y^0 y} \\ v^{ref,0}(x,y) &= A_{TE}^{-} e^{\imath k_x^0 x + \imath k_y^0 y} \end{aligned}$$

where A_{TE}^{-} is a constant term.

As this geometry lacks any dielectric material or inconsistencies in the planar surface, the entire incoming wave is reflected at an angle equivalent to the incoming angle, thus there exists only one boundary condition at the surface of the PEC. When $y = 0$, the total electric field vanishes, which allows us to solve for the coefficient of the reflected wave. For the TE polarization, the relationship of the electric and magnetic field is governed by Eq. 1.6, where:

$$\begin{aligned} \nabla \times H &= \imath w \varepsilon_i E \\ E &= \frac{1}{\imath w \varepsilon_i} (\nabla \times H) \\ E &= \frac{1}{\imath w \varepsilon_i} (\nabla \times v(x,y)) \\ E &= \frac{1}{\imath w \varepsilon_i} \left(\frac{\partial v}{\partial y}(x,y) \right) \end{aligned} \tag{5.1}$$

Now the boundary condition at the conducting surface can be applied to solve for the coefficient A_{TE}^{-}.

$$\begin{aligned} \frac{1}{\imath w \varepsilon_0} \left(\frac{\partial v^0}{\partial y}(x,y) \right) &= 0 \\ \frac{\partial v^{inc,0}}{\partial y}(x,y) + \frac{\partial v^{ref,0}}{\partial y}(x,y) &= 0 \\ -\imath k_y^0 e^{\imath k_x^0 x} &= -\imath k_y^0 A_{TE}^{-} e^{\imath k_x^0 x} \\ A_{TE}^{-} &= 1 \end{aligned}$$

Thus the equations for the incoming and reflected wave in the TE case for the simplified geometry are:

$$\begin{aligned} v^{inc,0}(x,y) &= e^{\imath k_x^0 x - \imath k_y^0 y} \\ v^{ref,0}(x,y) &= e^{\imath k_x^0 x + \imath k_y^0 y} \end{aligned}$$

5.1.2 Non-Layered: With Cavity

Now consider the existence of a rectangular cavity situated below the half plane, where the cavity can be either empty or filled with a dielectric material. The introduction of such a cavity to the problem changes the behavior of the wave at the surface, where the transmitted and scattered fields must now be considered. The equations for the incoming and reflected fields were provided in section 5.1.1, and the general equations for the transmitted and reflected fields will be determined by applying logic similar to that displayed in chapter three.

The methodology of separation of variables is again applied, where the same general formulas are considered:

$$\overline{\underline{X}}(x) = C_1 \sin(\sqrt{\lambda}x) + C_2 \cos(\sqrt{\lambda}x)$$
$$\overline{\underline{Y}}(y) = C_3 e^{\imath\sqrt{\lambda}y} + C_4 e^{-\imath\sqrt{\lambda}y}$$

The expressions previously determined in chapter three for $\overline{\underline{X}}(x)$ and $\overline{\underline{Y}}(y)$ were related to the case when the electric component was perpendicular to the xy-plane. For the TE polarization, the electric component is now parallel to the plane. Since the magnetic field does not vanish at the surface of the PEC plane, the properties bounding the normal component of this field must be considered. In performing this action, the general solution for both components reduce to:

$$\overline{\underline{X}}(x) = C_1 \cos(\sqrt{\lambda}x)$$
$$\overline{\underline{Y}}(y) = C_5 \cosh(\gamma_2(y+d))$$

Therefore the equation of the magnetic component of the wave inside the cavity for the TE case is:

$$v^{t,2}(x,y) \;=\; \sum_{n=0}^{\infty} A_n^{TE} \cos\left(\frac{n\pi}{L}x\right) \cosh\left(\gamma_2(y+d)\right)$$

Since there are no additional boundary constraints affecting the scattered field, the TE representation of this field is similar to the TM case, where:

$$v^{scat,0}(x,y) = \int_{-\infty}^{\infty} D_{TE}(\lambda)\, e^{-\alpha_0 y} e^{2\pi \imath \lambda x} d\lambda$$

Thus, the general equations for the magnetic field of each region is:

$$v^{inc,0}(x,y) = e^{\imath k_x^0 x - \imath k_y^0 y} \tag{5.2}$$

$$v^{ref,0}(x,y) = e^{\imath k_x^0 x + \imath k_y^0 y} \tag{5.3}$$

$$v^{scat,0}(x,y) = \int_{-\infty}^{\infty} D_{TE}(\lambda)\, e^{-\alpha_0 y} e^{2\pi \imath \lambda x} d\lambda \tag{5.4}$$

$$v^{t,2}(x,y) = \sum_{n=0}^{\infty} A_n^{TE} \cos\left(\frac{n\pi}{L} x\right) \cosh\left(\gamma_2 (y+d)\right) \tag{5.5}$$

5.2 Satisfying the Boundary Conditions

Now that the field equations have been determined for each region of the geometry, the boundary conditions must be considered to assure that the waves are continuous at each material interface. In this geometry, there exists only one boundary at the cavity aperture between region I and region III, and the boundary conditions are reduced to those described in chapter 3, equations 3.10 and 3.11.

Applying the boundary constraint relevant to the electric field at the cavity aperture yields a solution for the coefficient $D_{TE}(\lambda)$:

$$\begin{aligned}
\frac{1}{iw\varepsilon_0}\left(\frac{\partial v^0}{\partial y}(x,0)\right) &= \frac{1}{iw\varepsilon_2}\left(\frac{\partial v^2}{\partial y}(x,0)\right) \\
\varepsilon_2\frac{\partial v^{inc,0}}{\partial y}(x,0)+\varepsilon_2\frac{\partial v^{ref,0}}{\partial y}(x,0)+\varepsilon_2\frac{\partial v^{scat,0}}{\partial y}(x,0) &= \varepsilon_0\frac{\partial v^{t,2}}{\partial y}(x,0) \\
\varepsilon_2\frac{\partial v^{scat,0}}{\partial y}(x,0) &= \varepsilon_0\frac{\partial v^{t,2}}{\partial y}(x,0) \\
-\varepsilon_2\int_{-\infty}^{\infty}\alpha_0 D_{TE}(\lambda)\,e^{2\pi\imath\lambda x}d\lambda &= -\varepsilon_0\sum_{n=0}^{\infty}A_n^{TE}\gamma_2\cos\left(\frac{n\pi}{L}x\right)\sinh(\gamma_2 d) \\
-\varepsilon_2\mathcal{F}^{-1}\left(\alpha_0 D_{TE}(\lambda)\right) &= -\varepsilon_0\sum_{n=0}^{\infty}\tilde{A_n^{TE}}\gamma_2\cos\left(\frac{n\pi}{L}x\right) \\
D_{TE}(\lambda) &= \frac{\varepsilon_{r2}}{\alpha_0}\sum_{n=0}^{\infty}\tilde{A_n^{TE}}\gamma_2\mathcal{F}\left(\cos\left(\frac{n\pi}{L}x\right)\right) \qquad (5.6)
\end{aligned}$$

where $\tilde{A_n^{TE}} = A_n^{TE}\sinh(\gamma_2 d)$.

The boundary condition related to the magnetic field at the cavity aperture is addressed next, where:

$$\begin{aligned}
v^0(x,0) &= v^2(x,0) \\
v^{inc,0}(x,0)+v^{ref,0}(x,0)+v^{scat,0}(x,0) &= v^{t,2}(x,0) \\
2e^{\imath k_x^0 x}+\int_{-\infty}^{\infty}D_{TE}(\lambda)\,e^{2\pi\imath\lambda x}d\lambda &= \sum_{n=0}^{\infty}A_n^{TE}\cos\left(\frac{n\pi}{L}x\right)\cosh(\gamma_2 d) \\
2e^{\imath k_x^0 x}+\mathcal{F}^{-1}\left(D_{TE}(\lambda)\right) &= \sum_{n=0}^{\infty}\tilde{A_n^{TE}}\cos\left(\frac{n\pi}{L}x\right)\coth(\gamma_2 d)
\end{aligned}$$

Again the orthogonality conditions of this equation allow the equation at the opening of the cavity to be reduced to:

$$\begin{aligned}
&\int_0^L 2e^{\imath k_x^0 x}\cos\left(\frac{m\pi}{L}x\right)dx+\int_0^L\mathcal{F}^{-1}\left(D_{TE}(\lambda)\right)\cos\left(\frac{m\pi}{L}x\right)dx \\
&\qquad=\begin{cases}\tilde{A_m^{TE}}L\coth(\gamma_{2m}d) & \text{if } m=n=0\\ \tilde{A_m^{TE}}\frac{L}{2}\coth(\gamma_{2m}d) & \text{if } m=n>0\end{cases}
\end{aligned}$$

Performing a straight integration and utilizing Parseval's Theorem further results in:

$$\left(\frac{e^{\imath k_x^0 L+\imath m\pi}-1}{\imath k_x^0+\frac{\imath m\pi}{L}}+\frac{e^{\imath k_x^0 L-\imath m\pi}-1}{\imath k_x^0-\frac{\imath m\pi}{L}}\right)+\int_{-\infty}^{\infty} D_{TE}\left(\lambda\right)\overline{\mathcal{F}\left(\cos\left(\frac{m\pi}{L}x\right)\right)}d\lambda$$
$$=\begin{cases} A_m^{\tilde{TE}} L\coth\left(\gamma_{2m}d\right) & \text{if } m=n=0 \\ A_m^{\tilde{TE}}\frac{L}{2}\coth\left(\gamma_{2m}d\right) & \text{if } m=n>0 \end{cases}$$

Lastly, substituting in the value for $D_{TE}\left(\lambda\right)$ that was determined in equation 5.6, and rearranging the equation yields:

$$\left(\frac{e^{\imath k_x^0 L+\imath m\pi}-1}{\imath k_x^0+\frac{\imath m\pi}{L}}+\frac{e^{\imath k_x^0 L-\imath m\pi}-1}{\imath k_x^0-\frac{\imath m\pi}{L}}\right)$$
$$+\varepsilon_{r2}\sum_{n=0}^{\infty} A_n^{\tilde{TE}}\gamma_2\int_{-\infty}^{\infty}\frac{1}{\alpha_0}\mathcal{F}\left(\cos\left(\frac{n\pi}{L}x\right)\right)\overline{\mathcal{F}\left(\cos\left(\frac{m\pi}{L}x\right)\right)}d\lambda \tag{5.7}$$
$$=\begin{cases} A_m^{\tilde{TE}} L\coth\left(\gamma_{2m}d\right) & \text{if } m=n=0 \\ A_m^{\tilde{TE}}\frac{L}{2}\coth\left(\gamma_{2m}d\right) & \text{if } m=n>0 \end{cases}$$

The Fourier coefficients, $A_n^{\tilde{TE}}$, form a system of equations that can be solved for computationally by truncating the infinite sum to an arbitrarily large number. These solutions are then applied to solve for the equation at the cavity aperture.

Chapter 6

TE Case - Layered Geometry

In this chapter, the geometry of chapter five is extended to include a material layer above the half plane. Again we are considering the TE case, where we will first address the changes of the incoming and reflected fields based on the addition of the layer to the planar surface . Once these fields have been determined, the effect of the material layer when a rectangular cavity is embedded in the half plane is examined. These equations will then be used to determine a solution at the cavity opening.

6.1 Field Equations

6.1.1 Layered: No Cavity

As discussed in chapter four, even in a geometry lacking the cavity structure, the field equations must be re-examined because of the complexity that a material overlay adds to the problem. A series of coefficients are utilized to account for the the change in speed

and the angle of refraction when the wave passes from region I to region II, where the incoming and reflected waves of each these regions are:

$$\begin{aligned} v^{inc,0}(x,y) &= e^{\imath k_x^0 x - \imath k_y^0 y} \\ v^{ref,0}(x,y) &= A_{TE}^- e^{\imath k_x^0 x + \imath k_y^0 y} \\ v^{inc,1}(x,y) &= B_{TE}^+ e^{\imath k_x^1 x - \imath k_y^1 y} \\ v^{ref,1}(x,y) &= B_{TE}^- e^{\imath k_x^1 x + \imath k_y^1 y} \end{aligned}$$

Again, the boundary condition related to the PEC must be considered, where the electric field is known to vanish at this surface. This knowledge enables us to eliminate one of the unknown coefficients, where:

$$\begin{aligned} \frac{1}{\imath w \varepsilon_1}\left(\frac{\partial v^1}{\partial y}(x,0)\right) &= 0 \\ \frac{\partial v^{inc,1}}{\partial y}(x,0) &= -\frac{\partial v^{ref,1}}{\partial y}(x,0) \\ -k_y^1 B_{TE}^+ e^{\imath k_x^1 x} &= -k_y^1 B_{TE}^- e^{\imath k_x^1 x} \\ B_{TE}^+ &= B_{TE}^- \end{aligned}$$

To solve for the remaining coefficients, the boundary conditions related to the material layer at $y = a$ must be considered. As determined in section 2.2, the electric and magnetic fields are continuous across the interface, where applying the condition related to the electric field results in:

$$\begin{aligned} \frac{1}{\imath w \varepsilon_0}\left(\frac{\partial v^0}{\partial y}(x,a)\right) &= \frac{1}{\imath w \varepsilon_1}\left(\frac{\partial v^1}{\partial y}(x,a)\right) \\ \varepsilon_1 \frac{\partial v^{inc,0}}{\partial y}(x,a) + \varepsilon_1 \frac{\partial v^{ref,0}}{\partial y}(x,a) &= \varepsilon_0 \frac{\partial v^{inc,1}}{\partial y}(x,a) + \varepsilon_0 \frac{\partial v^{ref,1}}{\partial y}(x,a) \\ -\imath k_y^0 \varepsilon_1 e^{\imath k_x^0 x - \imath k_y^0 a} + \imath k_y^0 \varepsilon_1 A_{TE}^- e^{\imath k_x^0 x + \imath k_y^0 a} &= \imath k_y^1 \varepsilon_1 B_{TE}^+ \left(e^{\imath k_x^1 x + \imath k_y^1 a} - e^{\imath k_x^1 x - \imath k_y^1 a}\right) \end{aligned} \quad (6.1)$$

Assuring the the magnetic field is continuous at the material interface results in a similar equation:

$$\begin{aligned} v^0(x,a) &= v^1(x,a) \\ v^{inc,0}(x,a)+v^{ref,0}(x,a) &= v^{inc,1}(x,a)+v^{ref,1}(x,a) \\ e^{\imath k_x^0 x-\imath k_y^0 a}+A_{TE}^- e^{\imath k_x^0 x+\imath k_y^0 a} &= B_{TE}^+\left(e^{\imath k_x^1 x+\imath k_y^1 a}-e^{\imath k_x^1 x+\imath k_y^1 a}\right) \end{aligned} \tag{6.2}$$

These results provide us a system of equations in two unknowns that can be solved for, where:

$$A_{TE}^- = \frac{e^{-2\imath k_y^0 a}\left(-k_y^1\left(e^{\imath k_y^1 a}-e^{-\imath k_y^1 a}\right)-k_y^0\varepsilon_{r1}\left(e^{-\imath k_y^1 a}+e^{\imath k_y^1 a}\right)\right)}{k_y^1\left(e^{\imath k_y^1 a}-e^{-\imath k_y^1 a}\right)-k_y^0\varepsilon_{r1}\left(e^{-\imath k_y^1 a}+e^{\imath k_y^1 a}\right)} \tag{6.3}$$

$$B_{TE}^+ = \frac{-2k_y^0\varepsilon_{r1}e^{-\imath k_y^0 a}}{k_y^1\left(e^{\imath k_y^1 a}-e^{-\imath k_y^1 a}\right)-k_y^0\varepsilon_{r1}\left(e^{-\imath k_y^1 a}+e^{\imath k_y^1 a}\right)} \tag{6.4}$$

6.1.2 Layered: With Cavity

We now consider the TE case when an incident plane wave impinges on a rectangular cavity embedded in an infinite ground plane that has been entirely coated with a dielectric material. The field equations representing the incoming and reflected waves of region I and II were outlined in section 6.1.1, however the addition of the embedded cavity to the problem requires solutions for the transmitted and scattered fields.

Similar to the non-layered cavity problem presented in chapter four, the scattering equation of region I is :

$$v^{scat,0}(x,y) = \int_{-\infty}^{\infty} D_{TE}(\lambda)\, e^{-\alpha_0 y} e^{2\pi\imath\lambda x} d\lambda$$

Since region II is bounded both above and below, the scattering of the electromagnetic wave in the positive and negative direction must be accounted for, and is represented by:

$$v^{scat,1}(x,y) = \int_{-\infty}^{\infty} \left(G_{TE}(\lambda)\, e^{-\alpha_1 y} + H_{TE}(\lambda)\, e^{\alpha_1 y}\right) e^{2\pi\imath\lambda x} d\lambda$$

Lastly, the equation of the transmitted field is still represented by the same function determined in chapter five, when the material layer was not present.

$$v^{t,2}(x,y) = \sum_{n=0}^{\infty} A_n^{TE} \cos\left(\frac{n\pi}{L}x\right) \cosh\left(\gamma_2(y+d)\right)$$

Therefore, the magnetic field in each region can be represented by the following equations:

$$v^{inc,0}(x,y) = e^{\imath k_x^0 x - \imath k_y^0 y} \tag{6.5}$$

$$v^{ref,0}(x,y) = A_{TE}^{-} e^{\imath k_x^0 x + \imath k_y^0 y} \tag{6.6}$$

$$v^{scat,0}(x,y) = \int_{-\infty}^{\infty} D_{TE}(\lambda)\, e^{-\alpha_0 y} e^{2\pi\imath\lambda x} d\lambda \tag{6.7}$$

$$v^{inc,1}(x,y) = B_{TE}^{+} e^{\imath k_x^1 x - \imath k_y^1 y} \tag{6.8}$$

$$v^{ref,1}(x,y) = B_{TE}^{-} e^{\imath k_x^1 x + \imath k_y^1 y} \tag{6.9}$$

$$v^{scat,1}(x,y) = \int_{-\infty}^{\infty} \left(G_{TE}(\lambda)\, e^{-\alpha_1 y} + H_{TE}(\lambda)\, e^{\alpha_1 y}\right) e^{2\pi\imath\lambda x} d\lambda \tag{6.10}$$

$$v^{t,2}(x,y) = \sum_{n=0}^{\infty} A_n^{TE} \cos\left(\frac{n\pi}{L}x\right) \cosh\left(\gamma_2(y+d)\right) \tag{6.11}$$

6.2 Satisfying the Boundary Conditions

Now that the wave has a representation in each region, there are multiple boundary conditions that must be satisfied to assure continuity at each interface. These boundary conditions are stated in section 2.2, and the boundary condition when $y = a$ will first be addressed, followed by the boundary at $y = 0$, prior to solving for the Fourier coefficients.

6.2.1 Boundary $y = a$

As we have previously stated, the electric and magnetic fields are continuous across the material interface when $y = a$, thus the boundary conditions regulated by equations 2.2

and 2.4 must be applied. By first enforcing the constraint related to the electric component of the wave, Eq. 2.2, we are able to determine a solution for the coefficient $D_{TE}(\lambda)$:

$$\frac{1}{iw\varepsilon_0}\left(\frac{\partial v^0}{\partial y}(x,a)\right) = \frac{1}{iw\varepsilon_1}\left(\frac{\partial v^1}{\partial y}(x,a)\right)$$

$$\varepsilon_1\frac{\partial v^{inc,0}}{\partial y}(x,a) + \varepsilon_1\frac{\partial v^{ref,0}}{\partial y}(x,a) + \varepsilon_1\frac{\partial v^{scat,0}}{\partial y}(x,a)$$
$$= \varepsilon_0\frac{\partial v^{inc,1}}{\partial y}(x,a) + \varepsilon_0\frac{\partial v^{ref,1}}{\partial y}(x,a) + \varepsilon_0\frac{\partial v^{scat,1}}{\partial y}(x,a)$$

$$\varepsilon_1\frac{\partial v^{scat,0}}{\partial y}(x,a) = \varepsilon_0\frac{\partial v^{scat,1}}{\partial y}(x,a)$$

$$-\varepsilon_1\int_{-\infty}^{\infty}\alpha_0 D_{TE}(\lambda)\, e^{-\alpha_0 a}e^{2\pi\imath\lambda x}d\lambda = \varepsilon_0\int_{-\infty}^{\infty}\alpha_1\left(H_{TE}(\lambda)\, e^{\alpha_1 a} - G_{TE}(\lambda)\, e^{-\alpha_1 a}\right)e^{2\pi\imath\lambda x}d\lambda$$

$$\begin{aligned}
-\varepsilon_1\mathcal{F}^{-1}\left(\alpha_0 D_{TE}(\lambda)\, e^{-\alpha_0 a}\right) &= \varepsilon_0\mathcal{F}^{-1}\left(\alpha_1\left(H_{TE}(\lambda)\, e^{\alpha_1 a} - G_{TE}(\lambda)\, e^{-\alpha_1 a}\right)\right)\\
-\varepsilon_1\alpha_0 D_{TE}(\lambda)\, e^{-\alpha_0 a} &= \varepsilon_0\alpha_1 H_{TE}(\lambda)\, e^{\alpha_1} - \varepsilon_0\alpha_1 G_{TE}(\lambda)\, e^{-\alpha_1 a} \qquad (6.12)
\end{aligned}$$

Next, applying the boundary constraints controlling for the continuity of the magnetic field by Eq. 2.4 when also yields a solution for the coefficient $D_{TE}(\lambda)$:

$$\begin{aligned}
v^0(x,a) &= v^1(x,a)\\
v^{inc,0}(x,a) + v^{ref,0}(x,a) + v^{scat,0}(x,a) &= v^{inc,1}(x,a) + v^{ref,1}(x,a) + v^{scat,1}(x,a)\\
v^{scat,0}(x,a) &= v^{scat,1}(x,a)\\
\int_{-\infty}^{\infty} D_{TE}(\lambda)\, e^{-\alpha_0 a}e^{2\pi\imath\lambda x}d\lambda &= \int_{-\infty}^{\infty}\left(G_{TE}(\lambda)\, e^{-\alpha_1 a} + H_{TE}(\lambda)\, e^{\alpha_1 a}\right)e^{2\pi\imath\lambda x}d\lambda\\
\mathcal{F}^{-1}\left(D_{TE}(\lambda)\, e^{-\alpha_0 a}\right) &= \mathcal{F}^{-1}\left(G_{TE}(\lambda)\, e^{-\alpha_1 a} + H_{TE}(\lambda)\, e^{\alpha_1 a}\right)\\
D_{TE}(\lambda)\, e^{-\alpha_0 a} &= G_{TE}(\lambda)\, e^{-\alpha_1 a} + H_{TE}(\lambda)\, e^{\alpha_1 a} \qquad (6.13)
\end{aligned}$$

The results from these two boundary conditions provides a system of equations that can be used to solve for $G_{TE}(\lambda)$ and $H_{TE}(\lambda)$.

$$G_{TE}(\lambda) = D_{TE}(\lambda)\, e^{-\alpha_0 a}\left(\frac{e^{\alpha_1 a}\left(\varepsilon_0\alpha_1 + \varepsilon_1\alpha_0\right)}{2\varepsilon_0\alpha_1}\right) \qquad (6.14)$$

$$H_{TE}(\lambda) = D_{TE}(\lambda)\, e^{-\alpha_0 a}\left(\frac{e^{-\alpha_1 a}\left(\varepsilon_0\alpha_1 - \varepsilon_1\alpha_0\right)}{2\varepsilon_0\alpha_1}\right) \qquad (6.15)$$

6.2.2 Boundary $y = 0$

The remaining boundary condition at the cavity aperture is define by equations 2.1 and 2.3, which can now be applied to assure continuity of both the electric and magnetic fields across the material interface. Again, the behavior of the electric component, described by Eq 2.1, is addressed first, where:

$$\begin{aligned}
\frac{1}{iw\varepsilon_1}\left(\frac{\partial v^1}{\partial y}(x,0)\right) &= \frac{1}{iw\varepsilon_2}\left(\frac{\partial v^2}{\partial y}(x,0)\right) \\
\varepsilon_2\frac{\partial v^{inc,1}}{\partial y}(x,0)+\varepsilon_2\frac{\partial v^{ref,1}}{\partial y}(x,0)+\varepsilon_2\frac{\partial v^{scat,1}}{\partial y}(x,0) &= \varepsilon_1\frac{\partial v^{t,2}}{\partial y}(x,0) \\
\varepsilon_2\frac{\partial v^{scat,1}}{\partial y}(x,0) &= \varepsilon_1\frac{\partial v^{t,2}}{\partial y}(x,0) \\
\varepsilon_2\int_{-\infty}^{\infty}\alpha_1\left(H_{TE}(\lambda)-G_{TE}(\lambda)\right)e^{2\pi\imath\lambda x}d\lambda &= \varepsilon_1\sum_{n=0}^{\infty}A_n^{TE}\gamma_2\cos\left(\frac{n\pi}{L}x\right)\sinh\left(\gamma_2 d\right) \\
\varepsilon_2\mathcal{F}^{-1}\alpha_1\left(H_{TE}(\lambda)-G_{TE}(\lambda)\right) &= \varepsilon_1\sum_{n=0}^{\infty}\tilde{A_n^{TE}}\gamma_2\cos\left(\frac{n\pi}{L}x\right) \\
\varepsilon_2\alpha_1\left(H_{TE}(\lambda)-G_{TE}(\lambda)\right) &= \varepsilon_1\sum_{n=0}^{\infty}\tilde{A_n^{TE}}\gamma_2\mathcal{F}\left(\cos\left(\frac{n\pi}{L}x\right)\right)
\end{aligned}$$

As the values for for $G_{TE}(\lambda)$ and $H_{TE}(\lambda)$ were determined in the previous section, substituting in to this equation further reduces to:

$$\begin{aligned}
\varepsilon_2 D_{TE}(\lambda)\,e^{-\alpha_0 a}\frac{\left(e^{-\alpha_1 a}\left(\varepsilon_0\alpha_1-\varepsilon_1\alpha_0\right)-e^{\alpha_1 a}\left(\varepsilon_0\alpha_1+\varepsilon_1\alpha_0\right)\right)}{2\varepsilon_0} \\
= \varepsilon_1\sum_{n=0}^{\infty}\tilde{A_n^{TE}}\gamma_2\mathcal{F}\left(\cos\left(\frac{n\pi}{L}x\right)\right)
\end{aligned}$$

where we are now able to solve for $D_{TE}(\lambda)\,e^{-\alpha_0 a}$:

$$D_{TE}(\lambda)\,e^{-\alpha_0 a} = \frac{2\varepsilon_0\varepsilon_1\sum_{n=0}^{\infty}\tilde{A_n^{TE}}\gamma_2\mathcal{F}\left(\cos\left(\frac{n\pi}{L}x\right)\right)}{\varepsilon_2\mathcal{Q}_{\mathcal{A}}^{\mathcal{TE}}} \tag{6.16}$$

where

$$\mathcal{Q}_{\mathcal{A}}^{\mathcal{TE}} = e^{-\alpha_1 a}\left(\varepsilon_0\alpha_1-\varepsilon_1\alpha_0\right)-e^{\alpha_1 a}\left(\varepsilon_0\alpha_1+\varepsilon_1\alpha_0\right)$$

The behavior of the magnetic component across the cavity aperture when $y = 0$ is investigated next, where:

$$\begin{aligned} v^1(x,0) &= v^2(x,0) \\ v^{inc,1}(x,0) + v^{ref,1}(x,0) + v^{scat,1}(x,0) &= v^{t,2}(x,0) \\ 2B_{TE}^{+} e^{\imath k_x^1 x} + \int_{-\infty}^{\infty} \left(G_{TE}(\lambda) + H_{TE}(\lambda)\right) e^{2\pi\imath\lambda x} d\lambda &= \sum_{n=0}^{\infty} A_n^{TE} \cos\left(\frac{n\pi}{L}x\right) \cosh(\gamma_2 d) \\ 2B_{TE}^{+} e^{\imath k_x^1 x} + \mathcal{F}^{-1}\left(G_{TE}(\lambda) + H_{TE}(\lambda)\right) &= \sum_{n=0}^{\infty} \tilde{A_n^{TE}} \cos\left(\frac{n\pi}{L}x\right) \coth(\gamma_2 d) \end{aligned}$$

By applying the method relating to the orthogonality of the Fourier terms, the solution at the cavity opening then reduces to:

$$\begin{aligned} 2B_{TE}^{+} \int_0^L e^{\imath k_x^1 x} \cos\left(\frac{m\pi}{L}x\right) dx + \int_0^L \mathcal{F}^{-1}\left(G_{TE}(\lambda) + H_{TE}(\lambda)\right) \cos\left(\frac{m\pi}{L}x\right) dx \\ = \begin{cases} \tilde{A_m^{TE}} L \coth(\gamma_{2m} d) & \text{if } m = n = 0 \\ \tilde{A_m^{TE}} \frac{L}{2} \coth(\gamma_{2m} d) & \text{if } m = n > 0 \end{cases} \end{aligned}$$

Then by performing a straight integration and utilizing Parseval's Theorem, our results show:

$$\begin{aligned} B_{TE}^{+} \left(\frac{e^{\imath k_x^1 L + \imath m\pi} - 1}{\imath k_x^1 + \frac{\imath m\pi}{L}} + \frac{e^{\imath k_x^1 L - \imath m\pi} - 1}{\imath k_x^1 - \frac{\imath m\pi}{L}} \right) \\ = -\int_{-\infty}^{\infty} \left(G_{TE}(\lambda) + H_{TE}(\lambda)\right) \overline{\mathcal{F}\left(\cos\left(\frac{m\pi}{L}x\right)\right)} d\lambda \\ + \begin{cases} \tilde{A_m^{TE}} L \coth(\gamma_{2m} d) & \text{if } m = n = 0 \\ \tilde{A_m^{TE}} \frac{L}{2} \coth(\gamma_{2m} d) & \text{if } m = n > 0 \end{cases} \end{aligned}$$

Next, the values calculated for $G_{TE}(\lambda)$ and $H_{TE}(\lambda)$ can be substituting into the equation:

$$B^{+}_{TE}\left(\frac{e^{\imath k_x^1 L+\imath m\pi}-1}{\imath k_x^1+\frac{\imath m\pi}{L}}+\frac{e^{\imath k_x^1 L-\imath m\pi}-1}{\imath k_x^1-\frac{\imath m\pi}{L}}\right)$$
$$=-\int_{-\infty}^{\infty}\left(\frac{D_{TE}(\lambda)\,e^{-\alpha_0 a}\mathcal{Q}_{\mathcal{B}}^{\mathcal{TE}}}{2\varepsilon_0\alpha_1}\right)\overline{\mathcal{F}\left(\cos\left(\frac{m\pi}{L}x\right)\right)}d\lambda$$
$$+\begin{cases}\tilde{A_m^{TE}}L\coth(\gamma_{2m}d) & \text{if } m=n=0\\ \tilde{A_m^{TE}}\frac{L}{2}\coth(\gamma_{2m}d) & \text{if } m=n>0\end{cases}$$

where

$$\mathcal{Q}_{\mathcal{B}}^{\mathcal{TE}}=e^{-\alpha_1 a}(\varepsilon_0\alpha_1-\varepsilon_1\alpha_0)+e^{\alpha_1 a}(\varepsilon_0\alpha_1+\varepsilon_1\alpha_0)$$

And lastly, the value determined for $D_{TE}(\lambda)\,e^{-\alpha_1 a}$ in equation 6.16 can now be substituted in to the final equation:

$$B^{+}_{TE}\left(\frac{e^{\imath k_x^1 L+\imath m\pi}-1}{\imath k_x^1+\frac{\imath m\pi}{L}}+\frac{e^{\imath k_x^1 L-\imath m\pi}-1}{\imath k_x^1-\frac{\imath m\pi}{L}}\right)$$
$$=-\frac{\varepsilon_1}{\varepsilon_2}\sum_{n=0}^{\infty}\tilde{A_n^{TE}}\gamma_2\int_{-\infty}^{\infty}\frac{1}{\alpha_1}\mathcal{F}\left(\cos\left(\frac{n\pi}{L}x\right)\right)\overline{\mathcal{F}\left(\cos\left(\frac{m\pi}{L}x\right)\right)}\frac{\mathcal{Q}_{\mathcal{B}}^{\mathcal{TE}}}{\mathcal{Q}_{\mathcal{A}}^{\mathcal{TE}}}d\lambda$$
$$+\begin{cases}\tilde{A_m^{TE}}L\coth(\gamma_{2m}d) & \text{if } m=n=0\\ \tilde{A_m^{TE}}\frac{L}{2}\coth(\gamma_{2m}d) & \text{if } m=n>0\end{cases}\tag{6.17}$$

The Fourier coefficients, $\tilde{A_n^{TE}}$, form a system of equations that can be solved for computationally by truncating the infinite sum to an arbitrarily large number. These solutions are then applied to solve for the equation at the cavity aperture, which are used in the formulation of the radar cross section.

In the calculation for the Fourier coefficients in the TE polarization, there is a factor of $\frac{1}{\alpha_1}$, where the possibility of $\alpha_1=0$ exists. To account for this singularity in our calculation, the golden section method was utilized to predict at what values $\alpha_1=0$. The values were then used as the bounds in which to seperate the integral into multiple segments, allowing us to perform a piecewise integration.

Chapter 7

Radar Cross Section Results

A radar system uses a transmitter to emit short pulses of electromagnetic waves towards a target, and a receiver to record the strength of the return echo. A comparison of these two values are depicted in a radar cross section. The location of the receiver of this system can vary between the site emitting the source, or multiple locations not at the source. When the transmitter and receiver are positioned at the same location, the incident and reflective angles of the plane waves are equal and the RCS is termed monostatic. In the case that a multisite radar system is used, the reflective angles differ from the incident angle, and the RCS is termed bistatic. Numerical results for both types of systems are provided in chapter eight.

Once the cavity is illuminated by an incoming electromagnetic plane wave, the resulting effect is a scattering of the plane wave into the far field. Since we are interested in the intensity of the scattered energy, a technique must be employed to predict this quantity given the strength of the incoming wave and the cavity geometry. Since the cavity aperture lies within an infinite PEC, we can consider covering the opening with a conductor so that the image theory can be implemented. A surface can then be constructed

on top of the infinite plane to produce equivalent electric (J) and magnetic (K) sources, where:

$$\overline{J_1} = \hat{n} \times \overline{H_1} \tag{7.1}$$

$$\overline{K_1} = \overline{E_1} \times \hat{n} \tag{7.2}$$

Applying the image theory guarantees that the PEC plane can be removed and the combination of the original charge configuration that originally laid above the PEC and the image configuration is electrically equivalent to the original charge configuration in the presence of the PEC. This process eliminates the electric source, leaving a doubled magnetic source located along the cavity aperture. The far field components of the electric field are computed from the resulting sources, and from this the RCS is configured by taking the norm of the squared far field values (Peterson, Ray, and Mittra 1998).

The general form of the two-dimensional scattering cross section for the TM and TE polarization is

$$\sigma_{TM}(\phi, \phi^{inc}) = \lim_{\rho \to \infty} 2\pi\rho \frac{|E_z^s(\rho, \phi)|^2}{|E_z^{inc}(0,0)|^2} \tag{7.3}$$

$$\sigma_{TE}(\phi, \phi^{inc}) = \lim_{\rho \to \infty} 2\pi\rho \frac{|H_z^s(\rho, \phi)|^2}{|H_z^{inc}(0,0)|^2} \tag{7.4}$$

where (ρ, ϕ) are ordinary polar coordinates. An equivalent expression of these equations is:

$$\sigma_{TM}(\phi, \phi^{inc}) = \frac{k_0}{4} \left| \int \int \left(\eta J_z + K_x \sin\phi - K_y \cos\phi\right) e^{\imath k_0 (x' \cos(\phi + y' \sin(\phi)))} dx' dy' \right|^2 \tag{7.5}$$

$$\sigma_{TE}(\phi, \phi^{inc}) = \frac{k_0}{4} \left| \int \int \left(J_x \sin\phi - J_y \cos\phi - \frac{K_z}{\eta}\right) e^{jk(x' \cos\phi + y' \sin\phi)} dx' dy' \right|^2 \tag{7.6}$$

where $\eta = \sqrt{\frac{\mu_0}{\varepsilon_0}}$, J_x, J_y and J_z represents the electric current of the x, y and z components, K_x, K_y and K_z represents the magnetic current of the x, y and z components. Additionally, the value of y' is fixed, such that if there does not exist a material layer above the cavity surface, $y' = 0$, otherwise, $y' = a$ (Peterson, Ray, and Mittra 1998).

The results of the image process revealed that our radar cross section is a function of only magnetic sources at the cavity aperture, thus eliminating J from our equations. Additionally, the magnetic sources as determined by equation 7.1 are a function of the electric field. In the TM polarization, the electric field is invariant in the z direction, where the product of this function with the normal results in the magnetic sources only existing in the x direction. Likewise, for the TE polarization, the electric field is invariant in the x direction, which results in the magnetic sources existing in the z direction. Applying these facts reduces the equations representing the RCS to

$$\sigma_{TM}(\phi, \phi^{inc}) = \frac{k_0}{4}\left|\int K_x \sin\phi e^{\imath k_0(x'\cos\phi + y'\sin\phi)}dx'\right|^2 \tag{7.7}$$

$$\sigma_{TE}(\phi, \phi^{inc}) = \frac{k_0}{4}\left|\int \frac{K_z}{\eta} e^{ik_0(x'\cos\phi + y'\sin\phi)}dx'\right|^2 \tag{7.8}$$

Since double the magnetic source remains at the cavity aperture after applying the method of images, substituting in the electric field further reduces these equations to:

$$\sigma_{TM}(\phi, \phi^{inc}) = \frac{k_0}{4}\left|-2\int E^{TM} \sin\phi e^{\imath k_0(x'\cos\phi + y'\sin\phi)}dx'\right|^2 \tag{7.9}$$

$$\sigma_{TE}(\phi, \phi^{inc}) = \frac{k_0}{4}\left|2\int \frac{E^{TE}}{\eta} e^{ik_0(x'\cos\phi + y'\sin\phi)}dx'\right|^2 \tag{7.10}$$

These general equations for the RCS can be applied to each of the geometries discussed through this paper. Solving for the geometry discussed in chapter three, where we considered the TM plane wave scattering from a rectangular cavity in a surface that had not been covered with a material layer, results in:

$$\begin{aligned}\sigma_{TM}(\phi, \phi^{inc}) &= \frac{k_0}{4}\left|-2\int_0^L \sum_{n=0}^{\infty} A_n^{\tilde{TM}} \sin\left(\frac{n\pi}{L}x\right)\sin\phi e^{\imath k_0 x'\cos\phi}dx'\right|^2 \\ \sigma_{TM}(\phi, \phi^{inc}) &= \frac{k_0}{4}\left|-2\sin\phi\sum_{n=0}^{\infty} A_n^{\tilde{TM}} \int_0^L \sin\left(\frac{n\pi}{L}x\right) e^{\imath k_0 x'\cos\phi}dx'\right|^2\end{aligned} \tag{7.11}$$

Likewise, the calculation for the RCS when a TM plane wave scatters from an embedded rectangular cavity that has been coated with a dielectric material changes to include the material layer. The layer complicates these calculations since we can no longer integrate over the cavity aperture, but must consider the entire boundary condition when $y' = a$. Therefore, to calculate the RCS, we must integrate over the entire domain:

$$\begin{aligned}
\sigma_{TM}(\phi,\phi^{inc}) &= \frac{k_0}{4}\left|-2\int_{-\infty}^{\infty}\left(\int_{-\infty}^{\infty} D_{TM}(\lambda)\, e^{-\alpha_0 a} e^{2\pi\imath\lambda x'} d\lambda\right)\sin(\phi) e^{\imath k_0(x'\cos\phi + a\sin\phi)} dx'\right|^2 \\
\sigma_{TM}(\phi,\phi^{inc}) &= \frac{k_0}{4}\left|-2\sin(\phi) e^{\imath k_0 a\sin\phi}\int_{-\infty}^{\infty}\mathcal{F}^{-1}\left(D_{TM}(\lambda)\, e^{-\alpha_0 a}\right) e^{2\pi\imath\lambda x'} dx'\right|^2 \\
\sigma_{TM}(\phi,\phi^{inc}) &= \frac{k_0}{4}\left|-2\sin(\phi) e^{\imath k_0 a\sin\phi}\mathcal{F}\left(\mathcal{F}^{-1}\left(D_{TM}(\lambda)\, e^{-\alpha_0 a}\right)\right)\right|^2 \\
\sigma_{TM}(\phi,\phi^{inc}) &= \frac{k_0}{4}\left|-2\sin(\phi) e^{\imath k_0 a\sin\phi} D_{TE}(\lambda)\, e^{-\alpha_0 a}\right|^2 \\
\sigma_{TM}(\phi,\phi^{inc}) &= \frac{k_0}{4}\left|-2\sin(\phi) e^{\imath k_0 a\sin\phi}\frac{2\mu_0\alpha_1\sum_{n=1}^{\infty} A_n^{\tilde{TM}}\mathcal{F}\left(\sin\left(\frac{n\pi}{L}x\right)\right)}{\left(e^{-\alpha_1 a}\left(\mu_0\alpha_1 - \mu_1\alpha_0\right) + e^{\alpha_1 a}\left(\mu_0\alpha_1 + \mu_1\alpha_0\right)\right)}\right|^2
\end{aligned}$$

where $\lambda = \frac{-k_0\cos\phi}{2\pi}$.

In a similar analysis, the results for the TE polarization when a plane wave scatters from a rectangular cavity that does not have a material layer above the surface reveals:

$$\begin{aligned}
\sigma_{TE}(\phi,\phi^{inc}) &= \frac{k_0}{4}\left|\frac{2}{\imath w\varepsilon_2\sqrt{\frac{\mu_0}{\varepsilon_0}}}\int_0^L\sum_{n=0}^{\infty} A_n^{\tilde{TE}}\gamma_2\cos\left(\frac{n\pi}{L}x\right) e^{\imath k_0 x\cos\phi} dx'\right|^2 \\
\sigma_{TE}(\phi,\phi^{inc}) &= \frac{k_0}{4}\left|\frac{2}{\imath w\varepsilon_2\sqrt{\frac{\mu_0}{\varepsilon_0}}}\sum_{n=0}^{\infty} A_n^{\tilde{TE}}\int_0^L\gamma_2\cos\left(\frac{n\pi}{L}x\right) e^{\imath k_0 x\cos\phi} dx'\right|^2
\end{aligned}$$

Lastly, the calculation for the RCS when a TE plane wave scatters from an embedded rectangular cavity that has been coated with a dielectric material changes to include the

material layer must take into consideration the surface of the boundary condition when $y' = a$, therefore requiring that we integrate over the entire x' domain.

$$
\begin{aligned}
\sigma_{TE}(\phi, \phi^{inc}) &= \frac{k_0}{4}\left|\frac{2}{\imath w\varepsilon_0\sqrt{\frac{\mu_0}{\varepsilon_0}}}\int_{-\infty}^{\infty}\left(\int_{-\infty}^{\infty}-\alpha_0 D_{TE}(\lambda)\, e^{-\alpha_0 a}e^{2\pi\imath\lambda x'}d\lambda\right)e^{\imath k_0(x'\cos\phi\ +a\sin\phi)}dx'\right|^2 \\
\sigma_{TE}(\phi, \phi^{inc}) &= \frac{k_0}{4}\left|\frac{2e^{\imath k_0 a\sin\phi}}{\imath w\varepsilon_0\sqrt{\frac{\mu_0}{\varepsilon_0}}}\int_{-\infty}^{\infty}\mathcal{F}^{-1}\left(-\alpha_0 D_{TE}(\lambda)\, e^{-\alpha_0 a}\right)e^{2\pi\imath\lambda x'}dx'\right|^2 \\
\sigma_{TE}(\phi, \phi^{inc}) &= \frac{k_0}{4}\left|\frac{2e^{\imath k_0 a\sin\phi}}{\imath w\varepsilon_0\sqrt{\frac{\mu_0}{\varepsilon_0}}}\mathcal{F}\left(\mathcal{F}^{-1}\left(-\alpha_0 D_{TE}(\lambda)\, e^{-\alpha_0 a}\right)\right)\right|^2 \\
\sigma_{TE}(\phi, \phi^{inc}) &= \frac{k_0}{4}\left|\frac{-2e^{\imath k_0 a\sin\phi}}{\imath w\varepsilon_0\sqrt{\frac{\mu_0}{\varepsilon_0}}}\alpha_0 D_{TE}(\lambda)\, e^{-\alpha_0 a}\right|^2 \\
\sigma_{TE}(\phi, \phi^{inc}) &= \frac{k_0}{4}\left|\frac{-2e^{\imath k_0 a\sin\phi}\alpha_0}{\imath w\varepsilon_0\sqrt{\frac{\mu_0}{\varepsilon_0}}}\frac{2\varepsilon_0\varepsilon_1\sum_{n=0}^{\infty}\tilde{A_n^{TE}}\gamma_2\mathcal{F}\left(\cos\left(\frac{n\pi}{L}x\right)\right)}{\varepsilon_2\left(e^{-\alpha_1 a}\left(\varepsilon_0\alpha_1-\varepsilon_1\alpha_0\right)-e^{\alpha_1 a}\left(\varepsilon_0\alpha_1+\varepsilon_1\alpha_0\right)\right)}\right|^2
\end{aligned}
\tag{7.12}
$$

where $\lambda = \frac{-k_0\cos\phi}{2\pi}$.

Chapter 8

Numerical Results

In this chapter, the results of the Fourier method are analyzed. Sections 8.1 and 8.2 display the RCS signature for various test cases for the TM polarization, while sections 8.3 and 8.4 provide similar results for the TE polarization. The layered methodology suggested by this research was coded using Matlab®, and validation testing of the code is provided in sections 8.1 (TM) and 8.3 (TE) to assure the output can duplicate the signatures of known publications. In order to simulate a geometry lacking a material layer above the half plane, the material parameters of region II were set equal to those of region I.

Sections 8.2 and 8.4 address the resulting effect of a surface layer on the RCS. To maintain consistency in test parameters for each polarization, the following set of general test cases were implemented:

1. Increasing the dimension of the material layer
2. Increasing the cavity depth
3. Increasing the cavity length

Each of these test cases are based on either a monostatic or bistatic radar system, and will be noted within each description. The bistatic angle for each plot is varied with the

parameters of the test cavity, however all monostatic plots were computed using an incident angle ranging between $[0, \frac{\pi}{2}]$. Additionally, results when implementing the Fourier method that use the entire coefficient matrix and the reduced diagonal matrix are compared for various examples.

8.1 TM: Validation Testing

8.1.1 Bistatic RCS Plots

To test the validity of the software, this first case compares both the Fourier method and the rapid approximation technique to results published by Morgan (Morgan 1998). The following is a bistatic RCS plot with an incident angle of 80^o. The material parameters of region II are set equal to the material parameters of region I, and the cavity of region III is filled with a material where $\varepsilon_r = 16 - 5\imath$, $\mu_r = 4 - 1.25\imath$. The rectangular cavity has a length of 1.25 meters and a depth of 0.0625 meters. The results of the graph below are in agreement with previous literature.

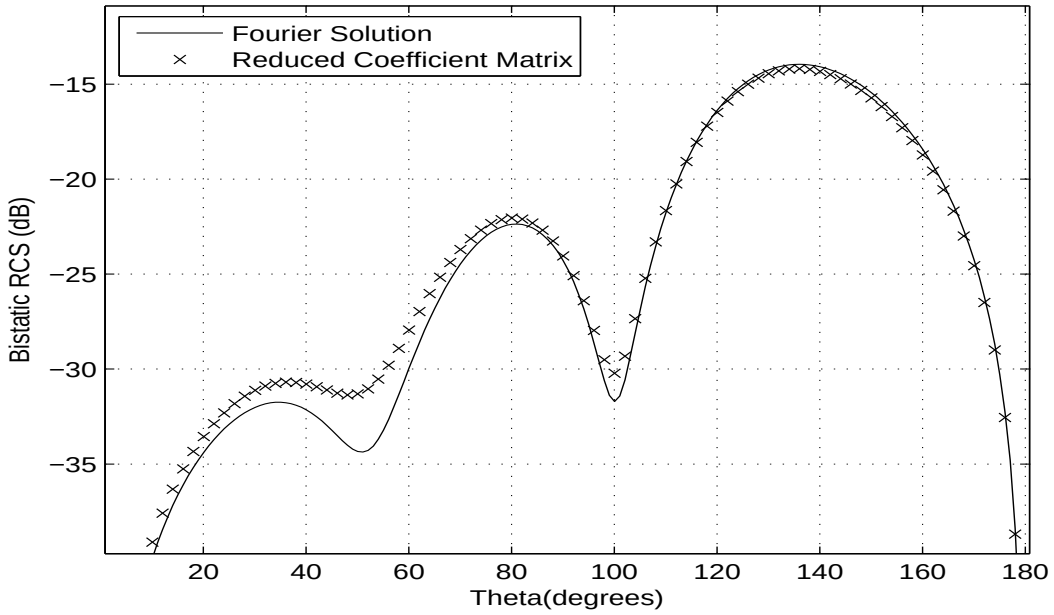

Figure 8.1: Bistatic RCS plot for TM incidence comparing the Fourier and fast approximation method when $\theta = 80^o$, $L = 1.25$, $d = 0.0625$, $\varepsilon_r = 16 - 5\imath$, $\mu_r = 4 - 1.25\imath$.

8.1.2 Monostatic RCS Plots

We again validate our program against results published by Morgan for the monostatic case, but this time consider testing a cavity with much larger dimensions. These results display the exact values using the Fourier method and the predict values using the fast approximation method. Here the cavity length is 10.2 meters and the cavity depth is 5.1 meters. The material parameters of the filled cavity are $\varepsilon_r = 4$ and $\mu_r = 1$. Note that the reduced coefficient calculations yielded the same RCS plot. Similar results are provided for the TE case in test cavity 7. Again, these results match the published literature.

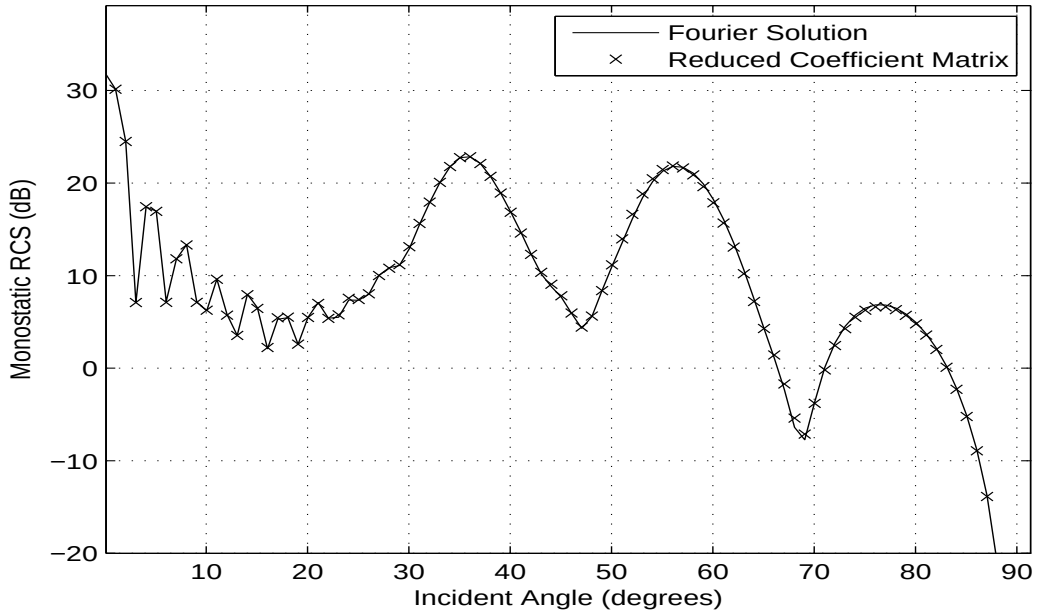

Figure 8.2: Monostatic RCS plot for TM incidence comparing the Fourier and fast approximation method when $L = 10.2$, $d = 5.1$, $\varepsilon_r = 4$, $\mu_r = 1$.

8.2 TM: Layered Geometry

8.2.1 Increasing Material Layer

Bistatic RCS Plots

Using the same parameters as those implemented in figure 8.1, the effects of increasing the material layer on the bistatic RCS are displayed below. The thickness of the material layer tested ranged from 0.025 to 0.075 meters for figure 8.3, while figure 8.4 considered larger variations ranging between 0.1 and 1.0 meters. Both of these results are compared to the geometry lacking a material layer above the half plane.

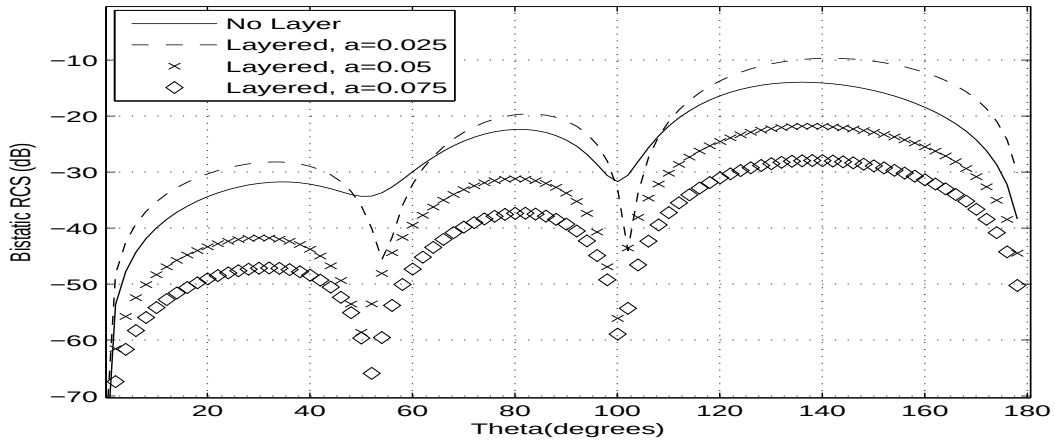

Figure 8.3: Bistatic RCS for TM polarization testing varying thickness parameters of the material surface, when $\theta = 80^o$, $L = 1.25$, $d = 0.0625$, $\varepsilon_r = 16 - 5\imath$, $\mu_r = 4 - 1.25\imath$.

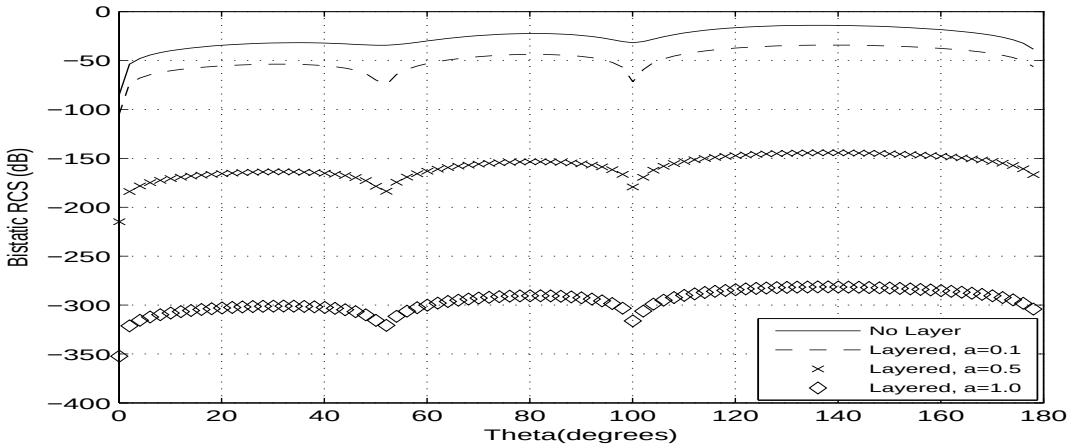

Figure 8.4: Bistatic RCS for TM polarization testing varying thickness parameters of the material surface, when $\theta = 80^o$, $L = 1.25$, $d = 0.0625$, $\varepsilon_r = 16 - 5\imath$, $\mu_r = 4 - 1.25\imath$.

Figures 8.5 and 8.6 analyze the effect of increasing the thickness of a nonconducting material layer on top of the infinite surface on the bistatic RCS. The electric permittivity and magnetic permeability of the medium tested are $\varepsilon_r = 4$ and $\mu_r = 1$, and the parameters representing the rectangular cavity below the half space are $L = 1.2$ and $d = 0.8$. Again, various parameters for the material thickness are tested, where figure 8.5 displays results comparing a range between 0.025 and 0.075 meters, and figure 8.6 displays the results for parameters ranging between 0.1 and 1.0.

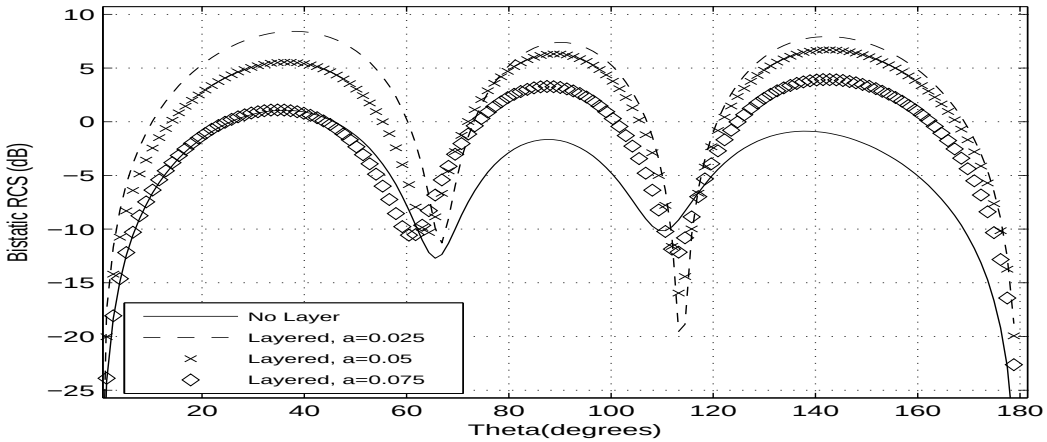

Figure 8.5: Bistatic RCS for TM polarization testing varying thickness parameters of the material surface, when $\theta = 60^o$, $L = 1.2$, $d = 0.8$, $\varepsilon_r = 4$, $\mu_r = 1$.

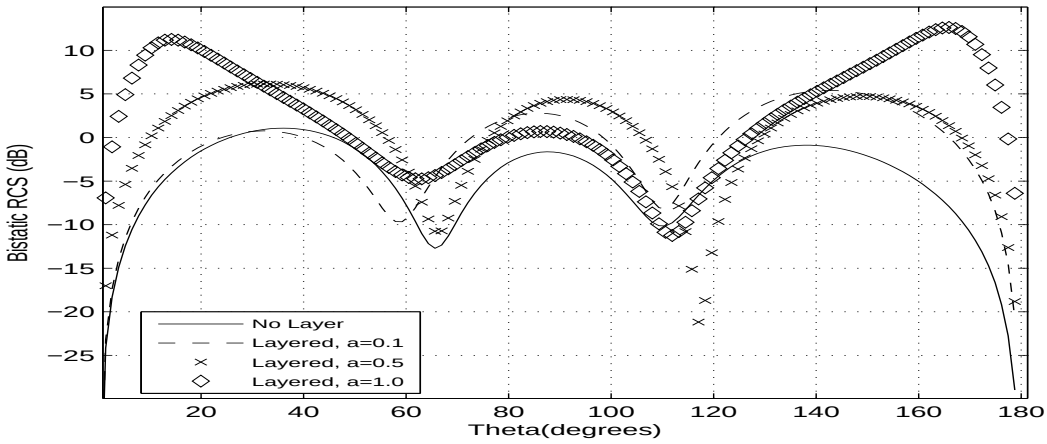

Figure 8.6: Bistatic RCS for TM Polarization testing varying thickness parameters of the material surface, when $\theta = 60^o$, $L = 1.2$, $d = 0.8$, $\varepsilon_r = 4$, $\mu_r = 1$.

Monostatic RCS Plots

Figures 8.7 and 8.8 display the results of altering the thickness of the material layer while holding all other parameters constant in a monostatic RCS plot for the TM polarization. The calculations considered an incident angle ranging between [0, $\frac{\pi}{2}$].

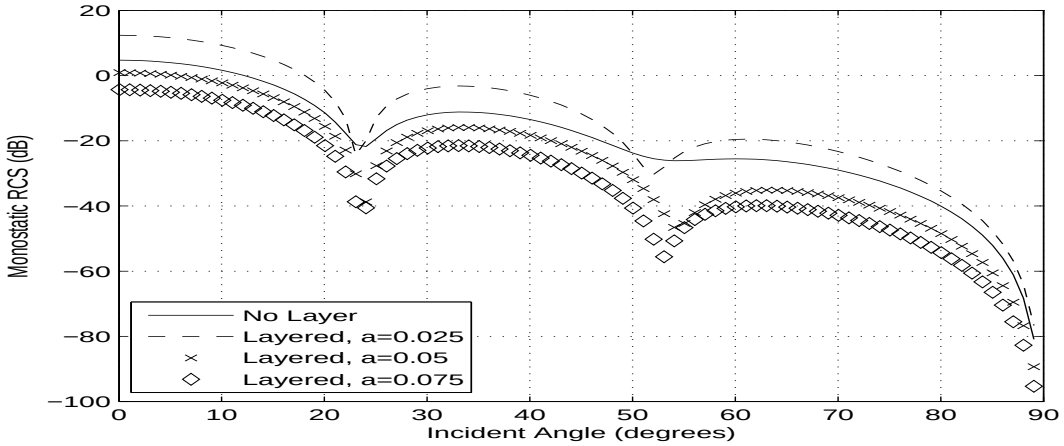

Figure 8.7: Monostatic RCS for TM polarization testing varying thickness parameters of the material surface, when $L = 1.25$, $d = 0.0625$, $\varepsilon_r = 16 - 5\imath$, $\mu_r = 4 - 1.25\imath$.

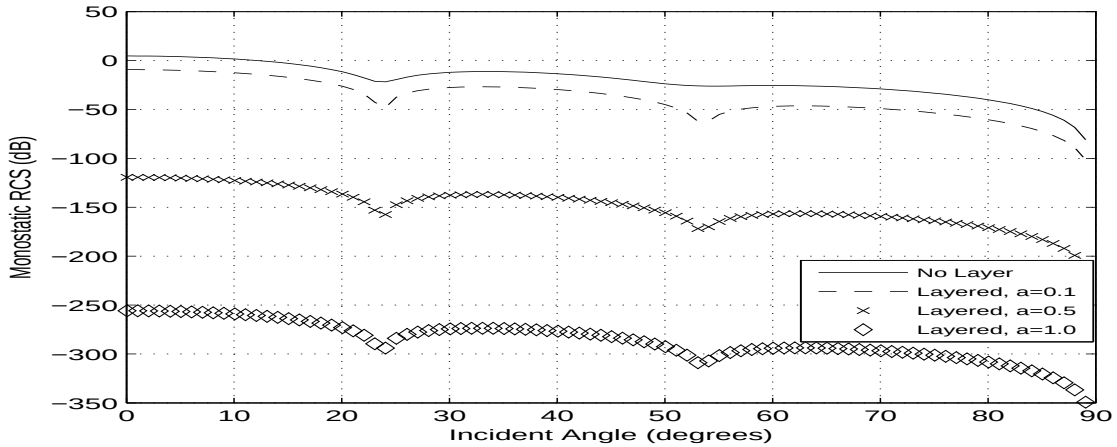

Figure 8.8: Monostatic RCS for TM polarization testing varying thickness parameters of the material surface, when $L = 1.25$, $d = 0.0625$, $\varepsilon_r = 16 - 5\imath$, $\mu_r = 4 - 1.25\imath$.

8.2.2 Increasing Cavity Depth

Bistatic RCS Plots

Figures 8.9 and 8.10 illustrate the effects of changing the cavity depth, given all other parameters held constant, on the bistatic RCS output. Figure 8.9 displays the results when applying a conducting material, while figure 8.10 displays the results incorporating a nonconducting material.

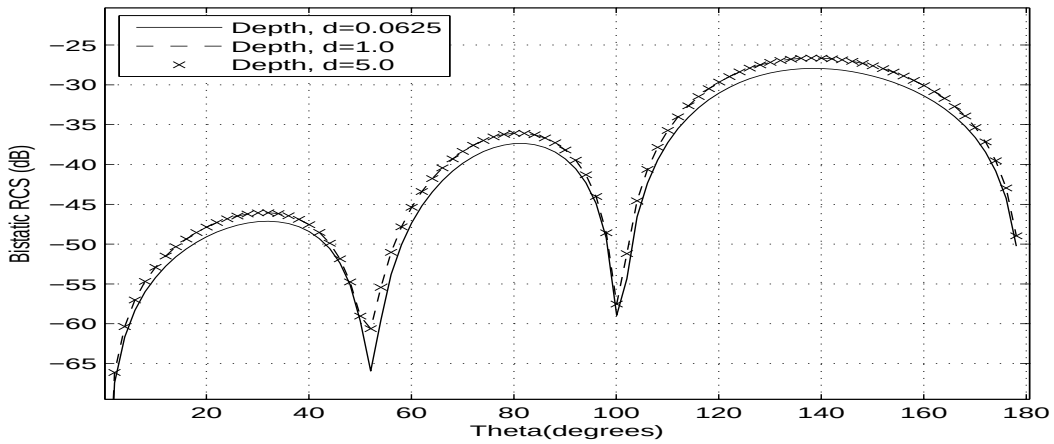

Figure 8.9: Bistatic RCS for TM polarization testing a varying cavity depth, when $\theta = 80^o$, $L = 1.25$, $a = 0.075$, $\varepsilon_r = 16 - 5\imath$, $\mu_r = 4 - 1.25\imath$.

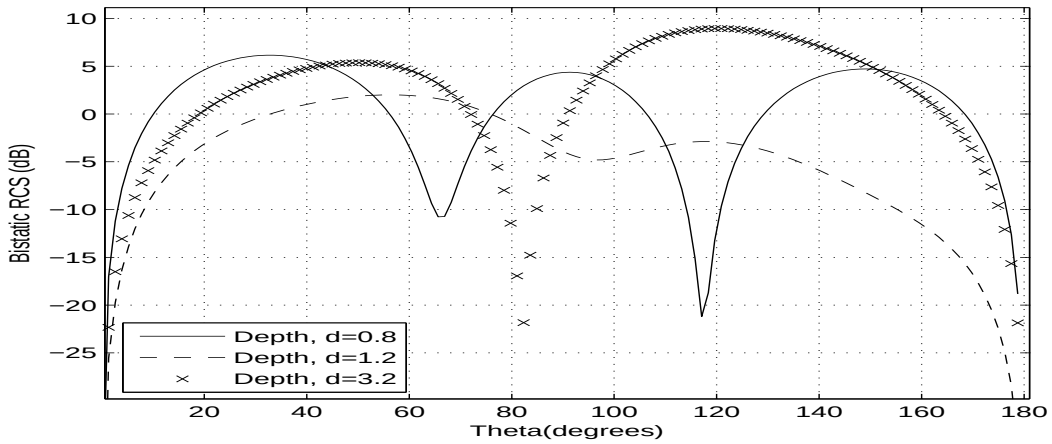

Figure 8.10: Bistatic RCS for TM polarization testing a varying cavity depth, when $\theta = 60^o$, $L = 1.2$, $a = 0.8$, $\varepsilon_r = 4$, $\mu_r = 1$.

Monostatic RCS Plots

Figure 8.11 displays the monostatic RCS output comparing various cavity depths when the material layer above the half plane consists of a conducting material.

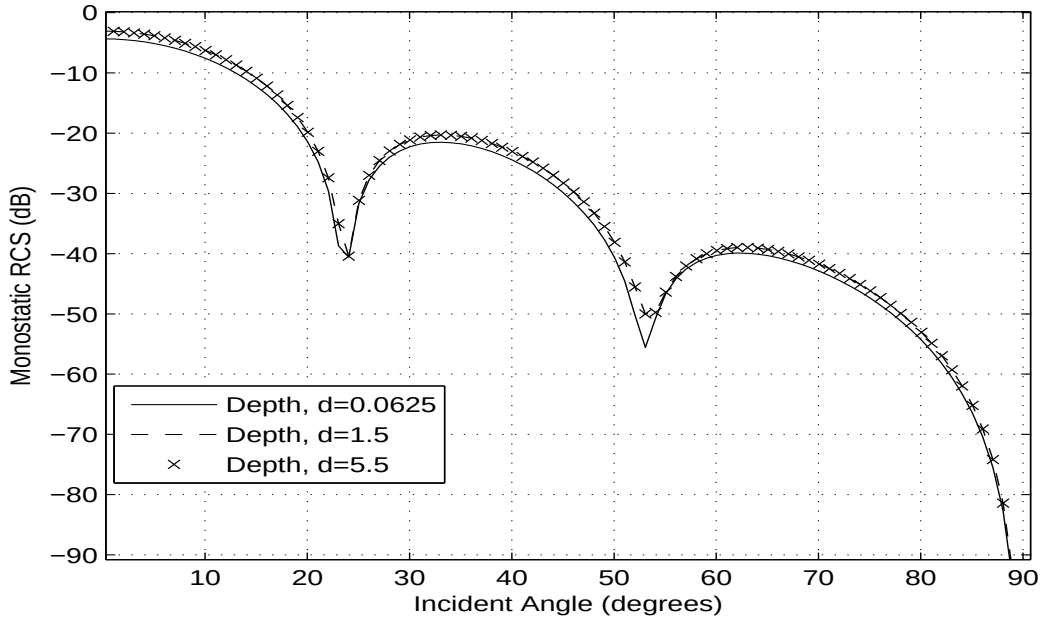

Figure 8.11: Monostatic RCS for TM polarization testing a varying cavity depth, when $L = 1.25$, $a = 0.075$, $\varepsilon_r = 16 - 5\imath$, $\mu_r = 4 - 1.25\imath$.

8.2.3 Increasing Cavity Width

Bistatic RCS Plots

For the next two RCS plots, varying lengths representing the cavity aperture were tested, while holding all remaining parameters constant. A conducting material was used to coat the rectangular cavity, as well as the surface above the half plane. As the length of the cavity aperture increases, the number of Fourier coefficients needed to assure that the solution converges increases, thus increasing the computational run time. Figure 8.12 uses the entire Fourier coefficient matrix to calculate the signature, and figure 8.13 reduces the run time by using only the diagonal matrix to compute the Fourier coefficients. As seen in the plots below, there is very little variation between these two methods, however the increase in the run time is significant. In the case of the longest cavity opening, when $L = 5.25$, the number of terms used to produce the output was $n = 80$. Using these dimensions, the runtime for the method implemented for figure 8.12 was 2677 seconds in comparison to the fast approximation method used for figure 8.13, which completed in 55 seconds.

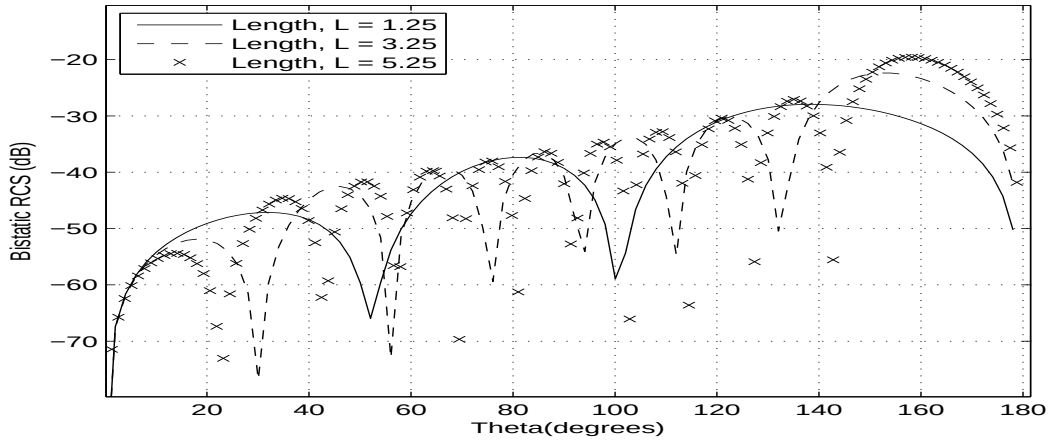

Figure 8.12: Bistatic RCS for TM polarization testing varying lengths of the cavity aperture, when $\theta = 80^o$, $d = 0.0625$, $a = 0.075$, $\varepsilon_r = 16 - 5\imath$, $\mu_r = 4 - 1.25\imath$. The exact Fourier method was applied.

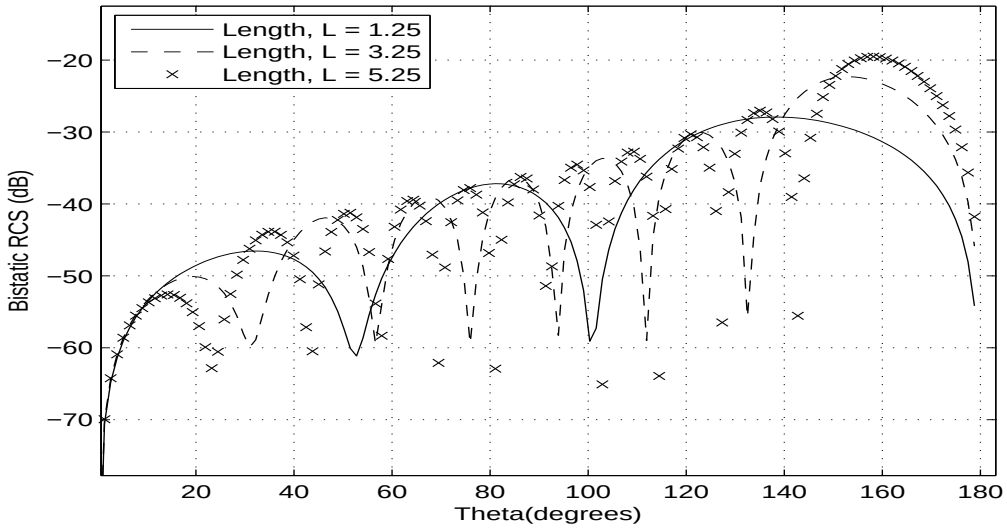

Figure 8.13: Bistatic RCS for TM polarization using the fast approximation method for testing varying cavity lengths, when $\theta = 80^o$, $d = 0.0625$, $a = 0.075$, $\varepsilon_r = 16 - 5\imath$, $\mu_r = -1.25\imath$.

The previous two figures illustrated the effect of varying the length of the cavity aperture when the surface was covered with conductive material. In comparison, the results of covering the surface with a non-conductive material are displayed below. Figure 8.14 utilized the exact Fourier method to produce the RCS, while figure 8.15 used the fast approximation technique to solve for the Fourier coefficients.

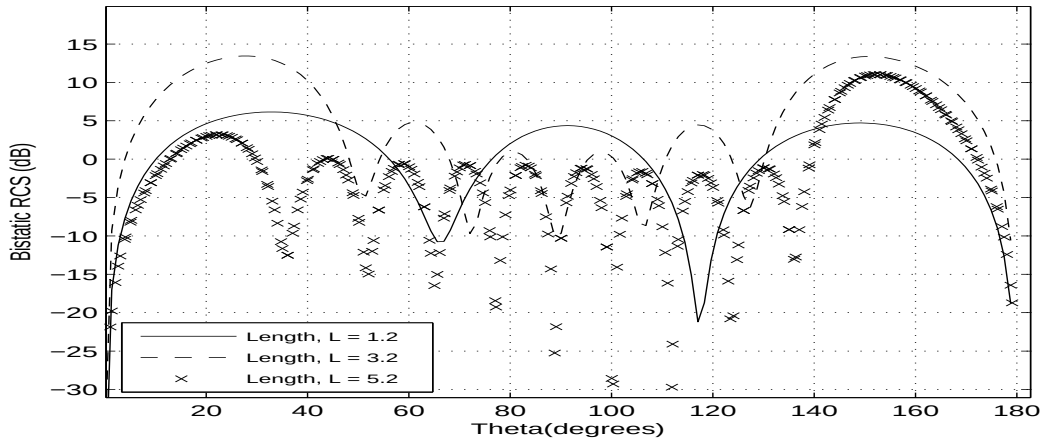

Figure 8.14: Bistatic RCS for TM polarization testing varying lengths of the cavity aperture, when $\theta = 60^o$, $d = 0.8$, $a = 0.5$, $\varepsilon_r = 4$, $\mu_r = 1$. The exact Fourier method was applied.

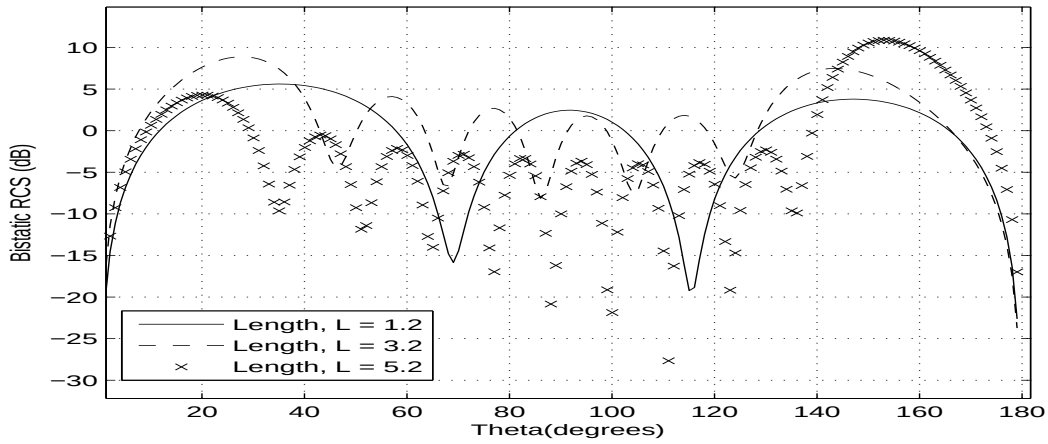

Figure 8.15: Bistatic RCS for TM polarization using the fast approximation method for testing varying cavity lengths, when $\theta = 60^o$, $d = 0.8$, $a = 0.5$, $\varepsilon_r = 4$, $\mu_r = 1$.

Monostatic RCS Plots

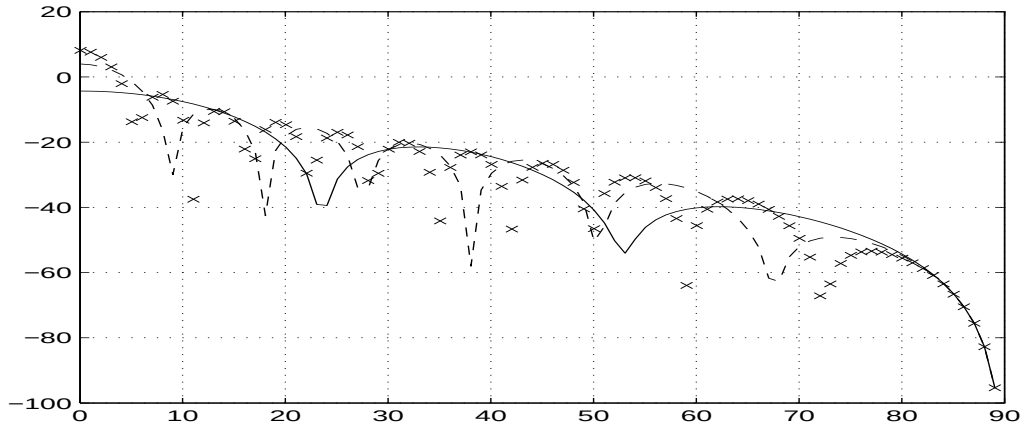

Figure 8.16: Monostatic RCS for TM polarization using the exact Fourier method for testing varying cavity lengths, when $d = 0.0625$, $a = 0.075$, $\varepsilon_r = 16 - 5\imath$, $\mu_r = 4 - 1.25\imath$.

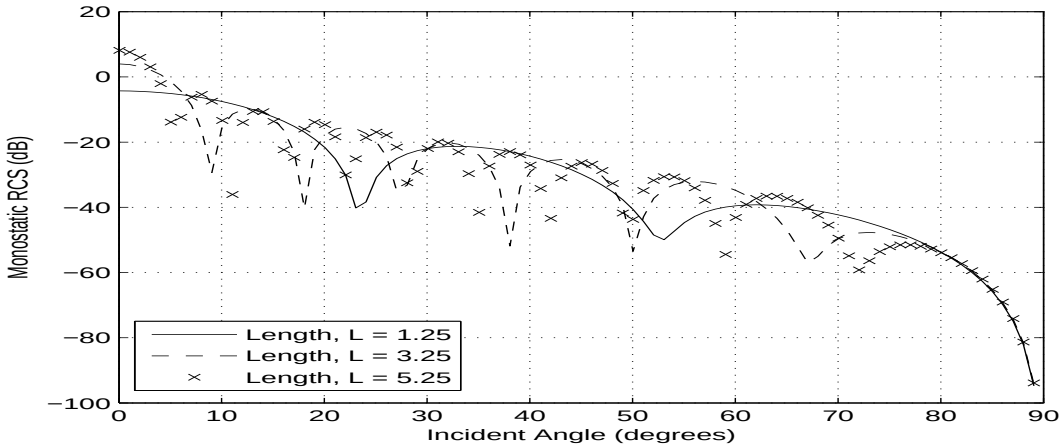

Figure 8.17: Monostatic RCS for TM polarization using the fast approximation method for testing varying cavity lengths, when $d = 0.0625$, $a = 0.075$, $\varepsilon_r = 16 - 5\imath$, $\mu_r = 4 - 1.25\imath$.

8.3 TE: Validation Testing

The validity of the software for the TE case is completed by setting the material parameters of region II equal to those of region I. The following is a bistatic RCS plot of a filled rectangular cavity where $\varepsilon_r = 16 - 5\imath$, $\mu_r = 4 - 1.25\imath$, $L = 1.25$ and $d = 0.0625$. The angle of the incoming plane wave is set to 80^o. The plot depicts the results using the complete Fourier methodology and the approximated technique, both which are in agreement with those previously published (Morgan 1998).

8.3.1 Bistatic RCS Plots

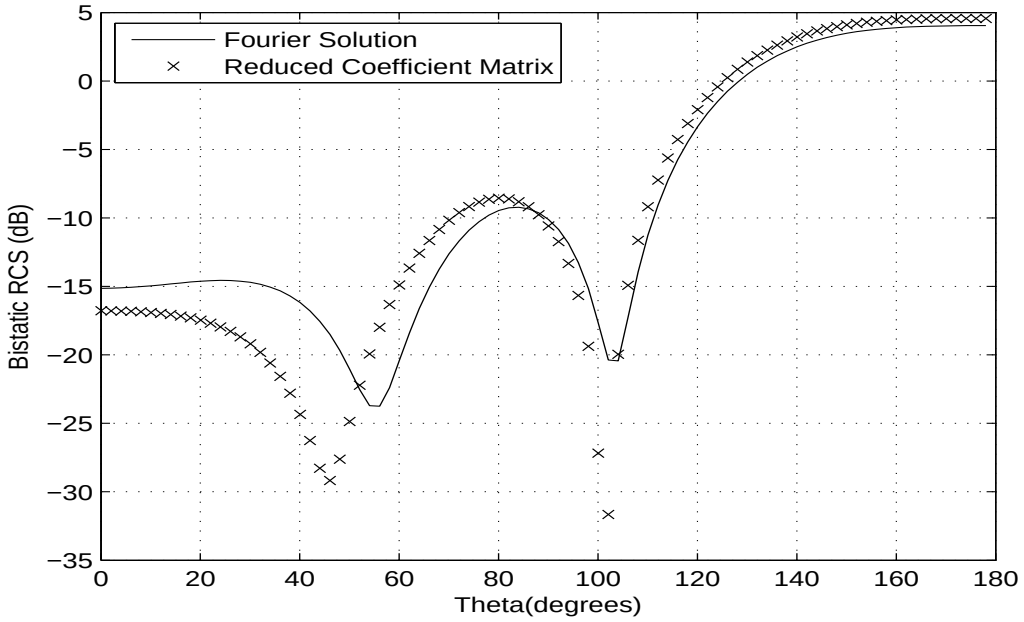

Figure 8.18: Bistatic RCS plot for TE incidence comparing the Fourier and fast approximation method when $\theta = 80^o$, $L = 1.25$, $d = 0.0625$, $\varepsilon_r = 16 - 5\imath$ and $\mu_r = 4 - 1.25\imath$.

8.3.2 Monostatic RCS Plots

We again validate our program against results published by Morgan for the TE monostatic case, but this time consider testing a cavity with much larger dimensions. Here the cavity length is 10.2 meters and the cavity depth is 5.1 meters. The material parameters of the filled cavity are $\varepsilon_r = 4$ and $\mu_r = 1$. These results match closely to the one published by Morgan, however there is a slight disagreement when $\theta^i \geq 70$.

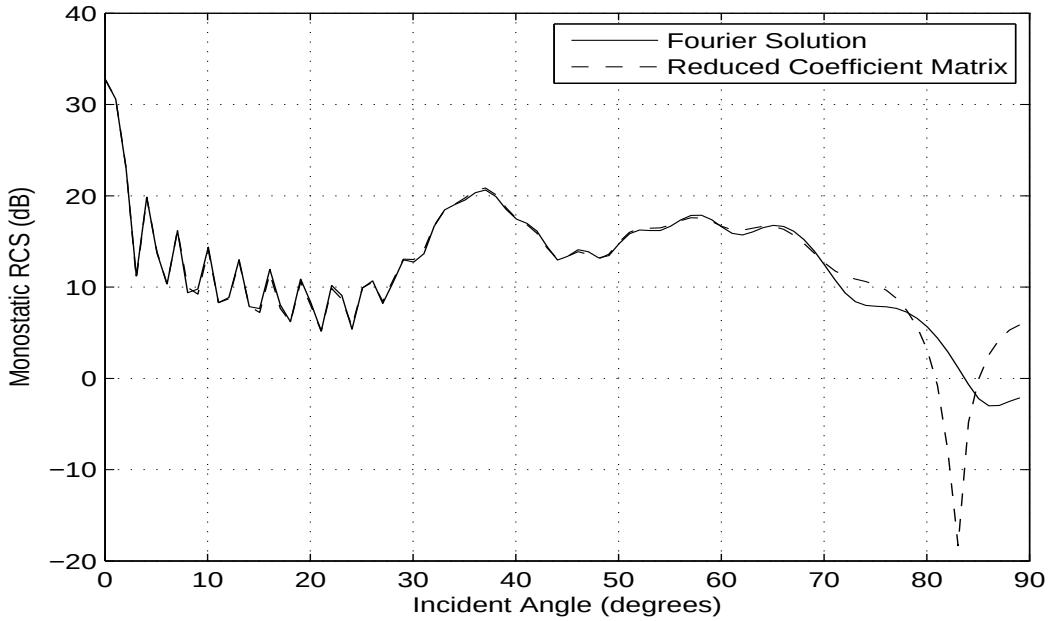

Figure 8.19: Monostatic RCS plot for TE incidence comparing the Fourier and fast approximation method when $L = 10.2$, $d = 5.1$, $\varepsilon_r = 4$, $\mu_r = 1$.

8.4 TE: Layered Geometry

8.4.1 Increasing Material Layer

Bistatic RCS Plots

The entire geometry described in figures 8.3 and 8.4 is repeated here for the TE polarization, where we are looking at increasing the thickness of the material coating the surface. When a conducing material is applied, the results for this polarization are similar, revealing that the strength of return echo tends to weaken as the material layer increases.

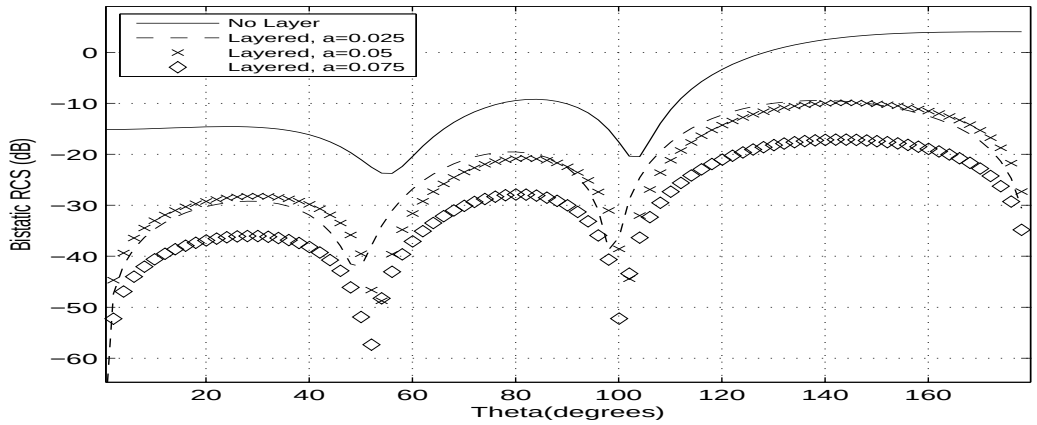

Figure 8.20: Bistatic RCS for TE polarization testing varying thickness parameters of the material surface, when $\theta = 80^o$, $L = 1.25$, $d = 0.0625$, $\varepsilon_r = 16 - 5i$, $\mu_r = 4 - 1.25i$.

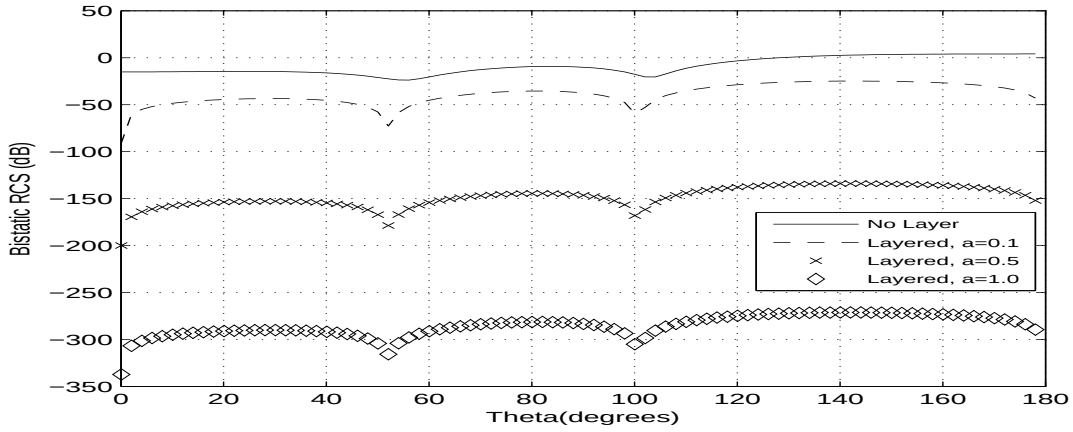

Figure 8.21: Bistatic RCS for TE polarization testing varying thickness parameters of the material surface, when $\theta = 80^o$, $L = 1.25$, $d = 0.0625$, $\varepsilon_r = 16 - 5i$, $\mu_r = 4 - 1.25i$.

Figures 8.22 and 8.23 displays the bistatic RCS for multiple values representing the material thickness, given all other parameters constant, where the surface consists of a nonconducting material.

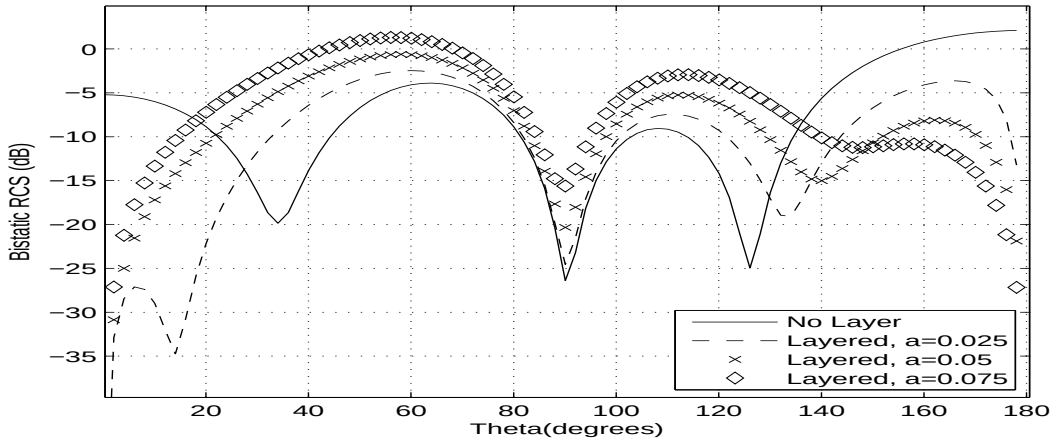

Figure 8.22: Bistatic RCS for TE polarization testing varying thickness parameters of the material surface, when $\theta = 60^o$, $L = 1.2$, $d = 0.8$, $\varepsilon_r = 4$, $\mu_r = 1$.

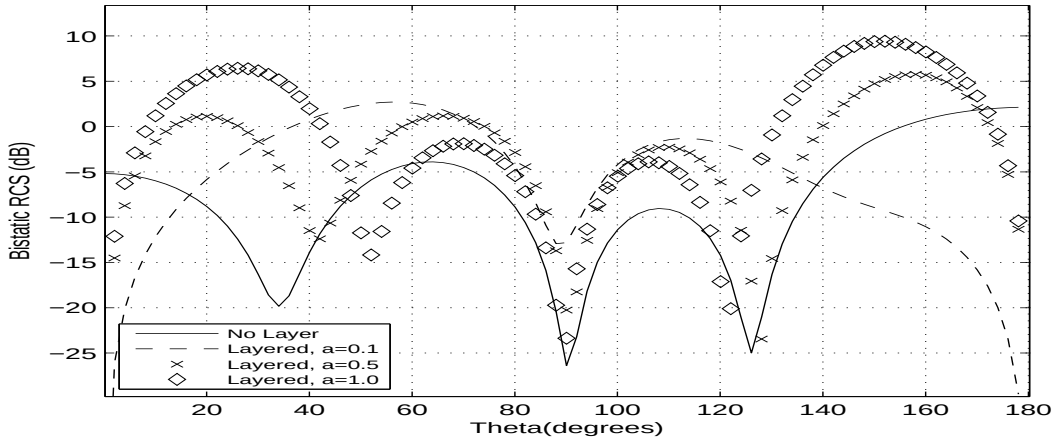

Figure 8.23: Bistatic RCS for TE polarization testing varying thickness parameters of the material surface, when $\theta = 60^o$, $L = 1.2$, $d = 0.8$, $\varepsilon_r = 4$, $\mu_r = 1$.

Monostatic RCS Plots

Figures 8.24 and 8.25 display the results of altering the thickness of the material layer while holding all other parameters constant in a monostatic RCS plot for the TE polarization. The calculations consider an incident angle ranging between $[0, \frac{\pi}{2}]$.

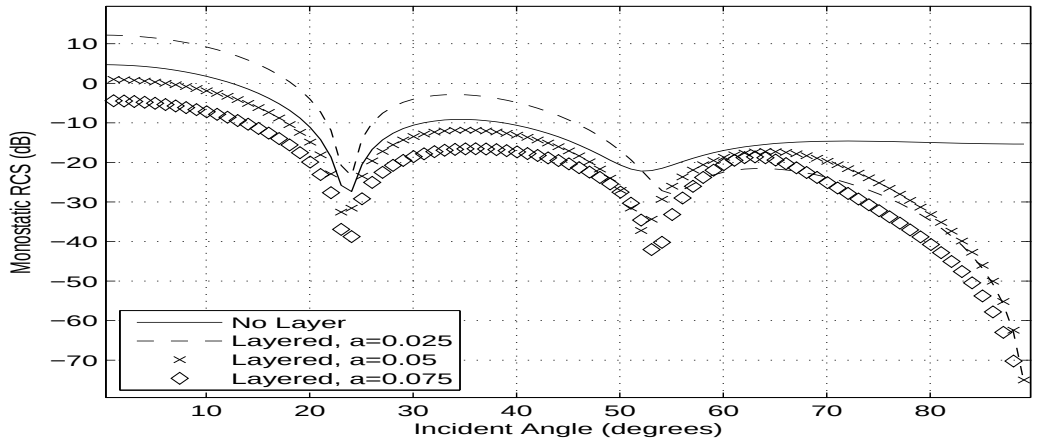

Figure 8.24: Monostatic RCS for TE Polarization, when $L = 1.25$, $d = 0.0625$, $\varepsilon_r = 16 - 5\imath$, $\mu_r = 4 - 1.25\imath$. Displays results for varying thickness values of the material surface.

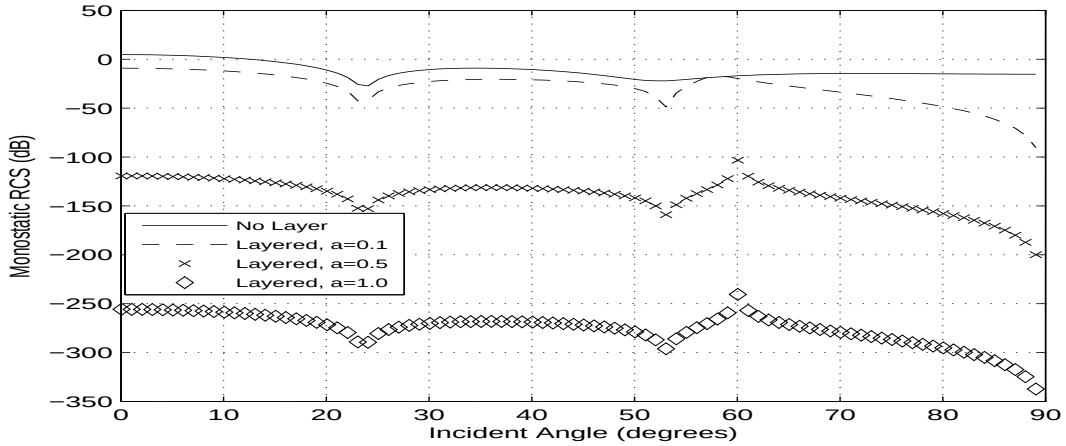

Figure 8.25: Monostatic RCS for TE Polarization, when $L = 1.25$, $d = 0.0625$, $\varepsilon_r = 16 - 5\imath$, $\mu_r = 4 - 1.25\imath$. Displays results for varying thickness values of the material surface.

8.4.2 Increasing Cavity Depth

Bistatic RCS Plots

Figures 8.26 and 8.27 illustrates the effect of a changing cavity depth, given all other parameters constant, on the bistatic RCS output. Figure 8.26 displays the results when applying a conducting material, while figure 8.27 displays the results incorporating a nonconducting material layer.

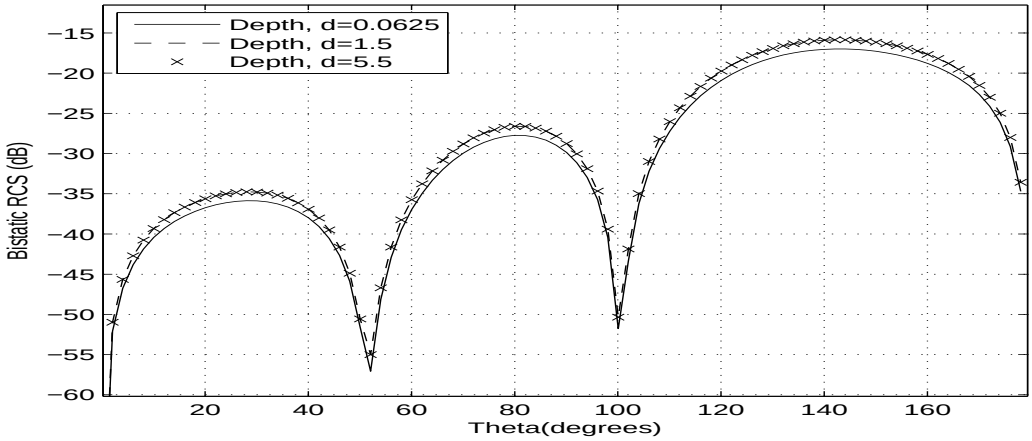

Figure 8.26: Bistatic RCS for TE polarization testing varying cavity depths, when $\theta = 80^o$, $L = 1.25$, $a = 0.075$, $\varepsilon_r = 16 - 5\imath$, $\mu_r = 4 - 1.25\imath$.

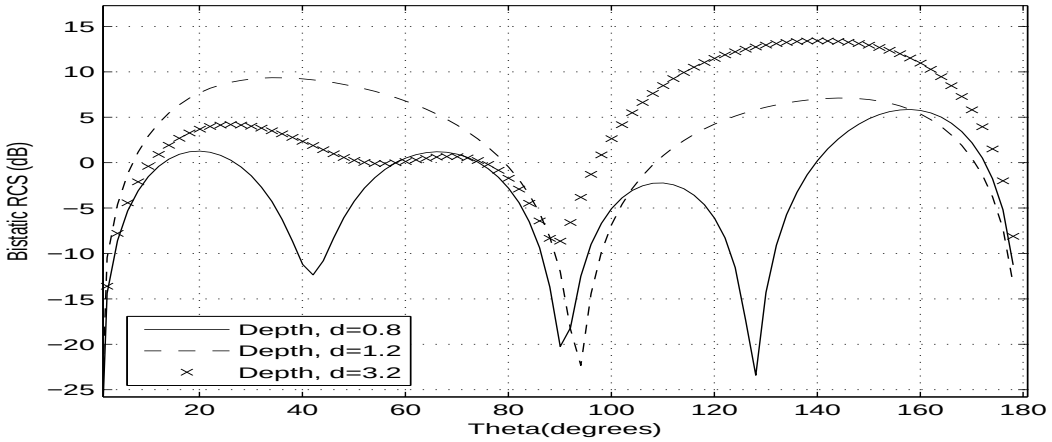

Figure 8.27: Bistatic RCS for TE polarization testing varying cavity depths, when $\theta = 60^o$, $L = 1.2$, $a = 0.5$, $\varepsilon_r = 4$, $\mu_r = 1$.

Monostatic RCS Plots

The effect of a changing cavity depth on a monostatic RCS plot of TE polarization is displayed in Figure 8.28.

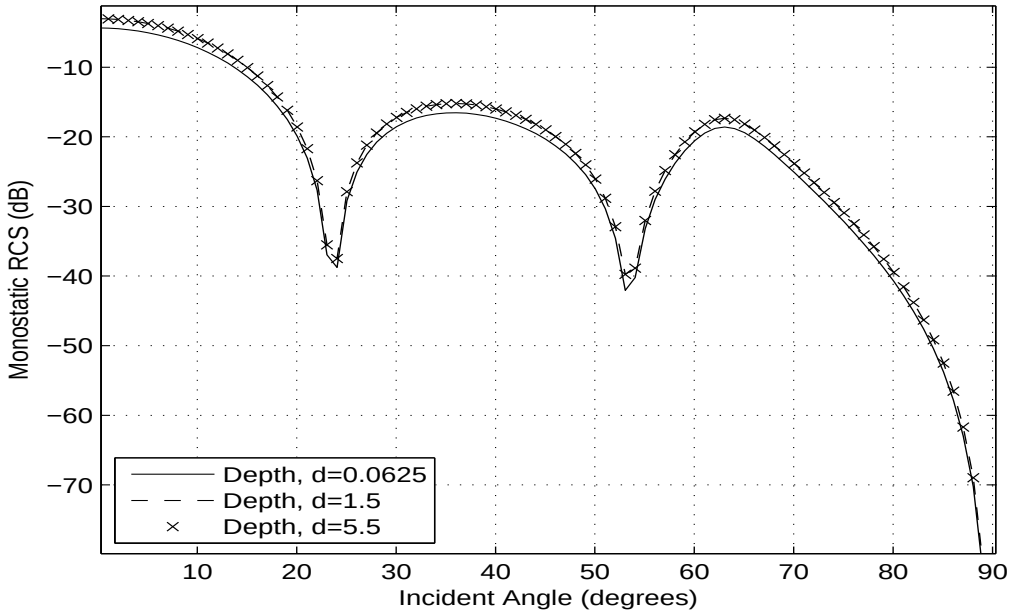

Figure 8.28: Monostatic RCS for TE Polarization testing varying thickness parameters of the material surface, when $L = 1.25$, $a = 0.075$, $\varepsilon_r = 16 - 5i$, $\mu_r = 4 - 1.25i$.

8.4.3 Increasing Cavity Width

Bistatic RCS Plots

Figures 8.29 and 8.30 display the results of increasing the length of the cavity aperture, holding all other parameters constant, when the entire geometry is coated with a conductive material. The figure in 8.29 reveals the approximation when using the restricted diagonal matrix when calculating the Fourier coefficients.

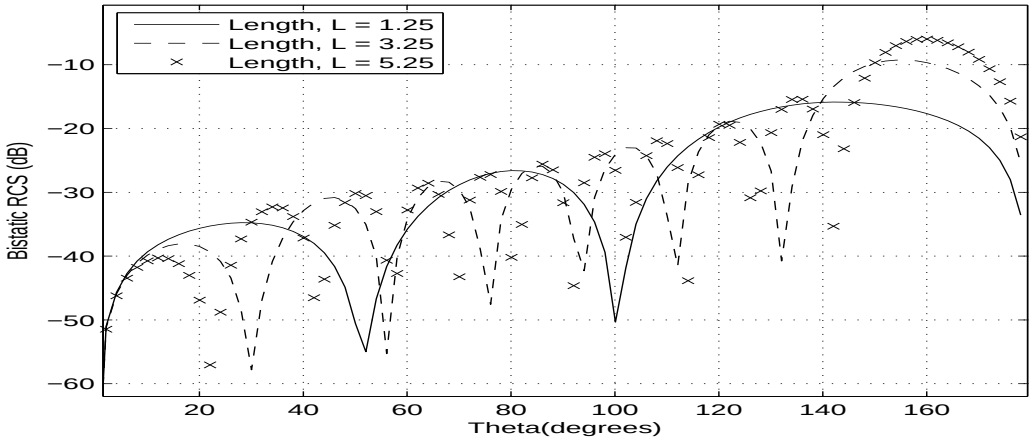

Figure 8.29: Bistatic RCS for TE polarization testing varying lengths of the cavity aperture, using the exact Fourier method. $\theta = 80^o$, $d = 0.0625$, $a = 0.075$, $\varepsilon_r = 16 - 5\imath$, $\mu_r = 4 - 1.25\imath$.

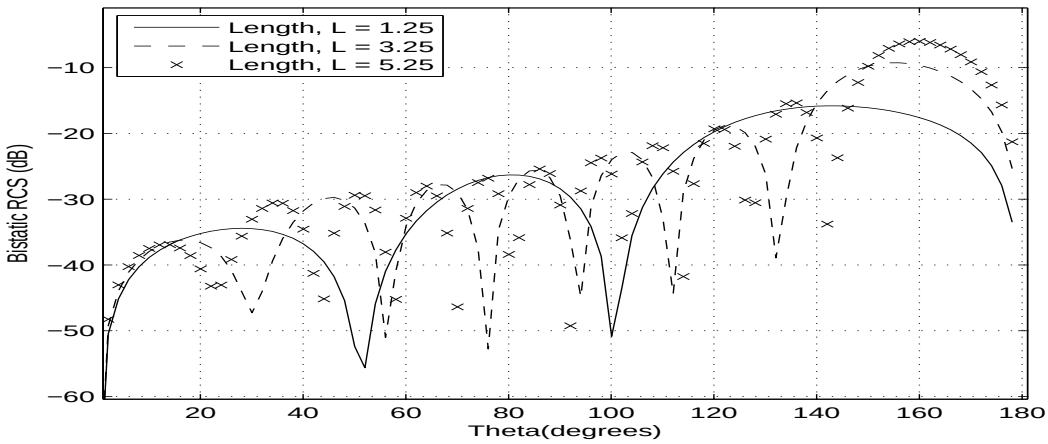

Figure 8.30: Bistatic RCS for TE polarization using the fast approximation method for testing varying lengths of the cavity aperture, when $\theta = 80^o$, $d = 0.0625$, $a = 0.075$, $\varepsilon_r = 16 - 5\imath$, $\mu_r = 4 - 1.25\imath$.

Results of an increasing cavity aperture when a non-conductive material is applied to the surface is displayed below in figures 8.31 and 8.32. The fast approximation technique was used to calculate the Fourier coefficients in figure 8.32.

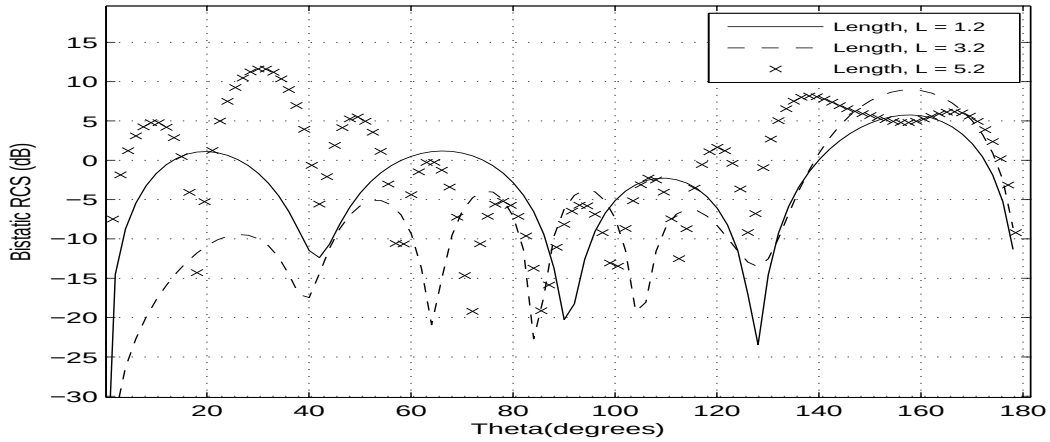

Figure 8.31: Bistatic RCS for TE polarization testing varying lengths of the cavity aperture while using the exact Fourier method, when $\theta = 60^o$, $d = 0.8$, $a = 0.5$, $\varepsilon_r = 4$, $\mu_r = 1$.

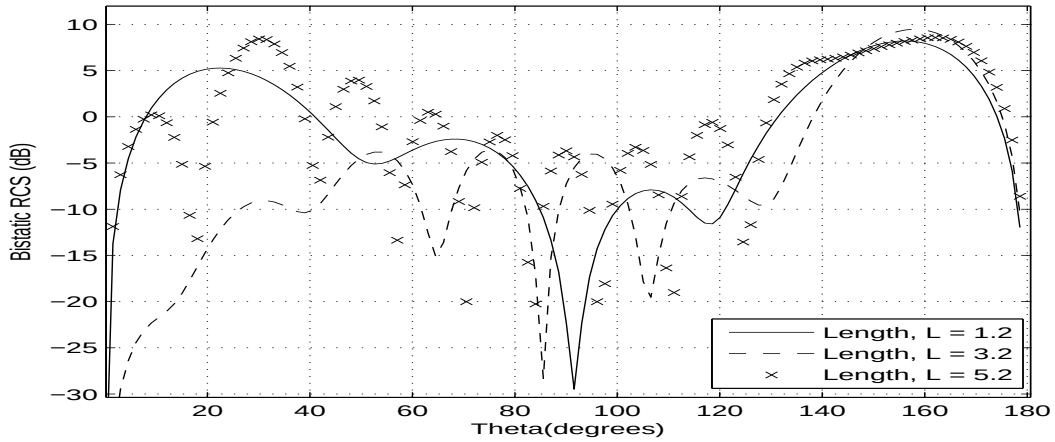

Figure 8.32: Bistatic RCS for TE polarization testing varying lengths of the cavity aperture while using the fast approximation method, when $\theta = 60^o$, $d = 0.8$, $a = 0.5$, $\varepsilon_r = 4$, $\mu_r = 1$.

Monostatic RCS Plots

Lastly, the figures displayed below compare the exact Fourier and fast approximation methods for monostatic RCS signatures.

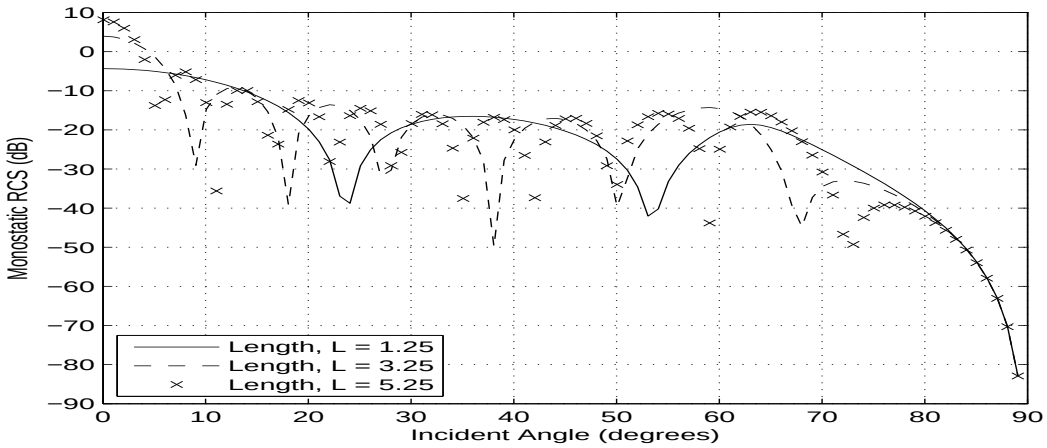

Figure 8.33: Monostatic RCS for TE polarization using the exact Fourier method, when $d = 0.0625$, $a = 0.075$, $\varepsilon_r = 16 - 5\imath$, $\mu_r = 4 - 1.25\imath$.

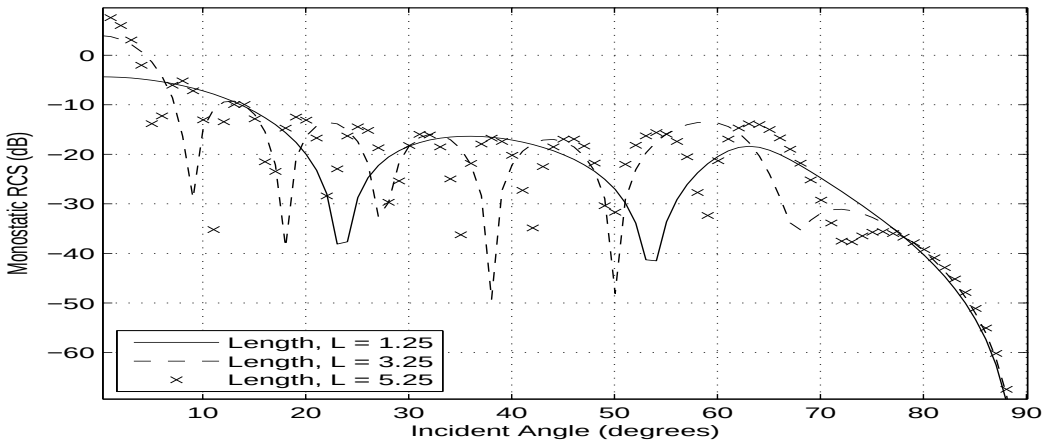

Figure 8.34: Monostatic RCS for TE polarization using the fast approximation method, when $d = 0.0625$, $a = 0.075$, $\varepsilon_r = 16 - 5\imath$, $\mu_r = 4 - 1.25\imath$.

Chapter 9

Conclusion and Future Work

In this publication, the Fourier transform technique was utilized to predict the far-field scattering of a rectangular cavity embedded in a dielectric covered infinite ground plane in two-dimensions. Methods solving for the transverse magnetic and transverse electric polarizations were both explored. The results offer an improvement to the accuracy of predicting radar cross sections.

In the examples displayed in chapter eight, the parameters defining the material coating above the half plane and inside the rectangular cavity present two types of materials, a conductive ($\varepsilon_r = 16 - 5\imath$, $\mu_r = 4 - 1.25\imath$) and non-conductive layer ($\varepsilon_r = 4$, $\mu_r = 1$). The results of coating the surface with a conductive material are similar for the TE and TM polarizations, with a trend showing that as the material layer thickens, the strength of the return echo weakens. This is consistent in the monostatic and bistatic signatures. Coating the surface with a non-conductive material results in an inconsistent behavior, however usually reveals an increase in the strength of the return signal. Analogous to the techniques explored by Morgan, the ability to decrease the computation time by restricting the coefficient matrix to the diagonal values was also incorporated as an option into the program. For most parameter combinations, this fast approximation method yielded results closely matching the predicted results. When time is a consideration, this

methodology offers a quick solution with a reasonable approximation.

There exists a number of avenues that are yet to be explored given this base model. One advancement is testing the effect of multiple material layers above the half plane on the output of the radar cross section. Additionally, the results presented here apply strictly when the shape of the cavity is rectangular, thus a natural progression would be the exploration of a methodology to be used for an arbitrarily shaped cavity. One last recommendation, as these results are approximations of a two-dimensional structure, there is an additional challenge to extend this work in three-dimensions.

Works Cited

Barkeshli, Kasra and John L. Volakis. Scattering by an Aperature formed by a Rectangular Cavity in a Ground Plane. Technical report, University of Michigan Radiation Laboratory Report 389757-2-T, December 1989.

Blackshire, James L., Charles Buynak, Gary Steffes, and Rob Marshall. "Nondestructive evaluation through aircraft coatings: a state-of-the-art assessment." *Joint FAA/DoD/NASA Aging Aircraft Conference*. March 2006.

Fleming, John. "Convergence Analysis of a Fourier-Based Solution Method of the Laplace Equation for a Model of Magnetic Recording." *Mathematical Problems in Engineering* 2008 (2008): 11 pages.

Hoppe, Daniel J. and Yahya Rahmat-Samii. *Impedance Boundary Conditions In Electromagnetics*. Washington DC: Taylor & Francis, 1995.

Howe, Eric. Analysis and Numerical Solution of an Integral Equation Method for Electromagnetic Scattering from a Cavity in a Ground Plane. Master's thesis, Air Force Institute of Technology, April 2001.

Morgan, M. A. "Mode Expansion Solution for Scattering by a Material Filled Rectangular Groove." *Progress In Electromagnetics Research* 98 (1998): 1–17.

Park, Tah J., Hyo J. Eom, and Kuniaki Yoshitomi. "An analytic solution for transverse-magnetic scattering from a rectangular channel in a conducting plane." *J. Appl. Phys.* 73 (1992): 3571–3573.

Park, Tah J., Hyo J. Eom, and Kuniaki Yoshitomi. "An analysis of TE-scattering from a rectangular channel in a conducting plane." *Radio Science* 28 (1993): 663–673.

Peterson, Andrew F., Scott L. Ray, and Raj Mittra. *Computational Methods for Electromagnetics*. New York: Institute of Electrical and Electronics Engineers, Inc., 1998.

Skolnik, Merrill. "An Introduction and Overview of Radar." *Radar Handbook. .* Cambridge: McGraw Hill, 1990.

Van, Tri and Aihua Wood. “Finite Element Analysis of Electromagnetic Scattering From a Cavity.” *IEEE Transactions on Antennas and Propagation* 51 (January 2003): 130–137.

Wood, Aihua. “Analysis of electromagnetic scattering from an overfilled cavity in the ground plane.” *Journal of Computational Physics* 215 (2006): 630–641.

Wood, William. *Electromagnetic Scattering from a Cavity in a Ground Plane: Theory and Experiment*. PhD thesis, Air Force Institute of Technology, March 1999.